JPL PUBLICATION 84-20

Multisensor Satellite Data Integration for Sea Surface Wind Speed and Direction Determination

Final Report

David L. Glackin
Gregory G. Pihos
Sherry L. Wheelock

March 30, 1984

Prepared for
U.S. Department of the Navy
Naval Environmental Prediction
Research Facility
Through an agreement with
National Aeronautics and Space Administration
by
Jet Propulsion Laboratory
California Institute of Technology
Pasadena, California

JPL PUBLICATION 84-20

Multisensor Satellite Data Integration for Sea Surface Wind Speed and Direction Determination

Final Report

David L. Glackin
Gregory G. Pihos
Sherry L. Wheelock

March 30, 1984

Prepared for

U.S. Department of the Navy
Naval Environmental Prediction
Research Facility

Through an agreement with

National Aeronautics and Space Administration

by

Jet Propulsion Laboratory
California Institute of Technology
Pasadena, California

The research described in this publication was performed by the Jet Propulsion Laboratory, California Institute of Technology, and was sponsored by the U.S. Department of the Navy through an agreement with the National Aeronautics and Space Administration.

PREFACE

This report covers work performed by the Jet Propulsion Laboratory (JPL) Image Processing Applications and Development Section (384) for the Naval Environmental Prediction Research Facility, Monterey, California. The JPL contract reference is Task Order No. RE-182/A179, Proposal No. 80-2120.

ACKNOWLEDGMENTS

The activities described in this report represent the combined effort of many people. Nevin Bryant of the Earth Resources Applications Group acquired the funding and provided valuable guidance. David Nichols was the original Task Manager and performed the initial site selection, wrote the software specification, and carried out some software development. Boris Gokhman, Ron McLeod, and Chris Pettus provided excellent programming and analysis support. Steve Adams' work was particularly outstanding in this regard. Jerry Clark assisted in data-ordering and formats. Technical discussions with many people in the field are gratefully acknowledged. Drs. Dudley Chelton, William Gray, Bruce Mendenhall, and Donald Wiley were especially helpful throughout the project. Special thanks are extended to the NEPRF contract monitors, Dr. Eve Schwartz and Roland Nagle. Finally, Elizabeth Davis and Trudy Grannell lent excellent typing support.

DLG wrote Sections 2-6 of this report and managed the task. GGP wrote Section 7, and jointly wrote Sections 1 and 8 with DLG. SLW led the software effort for all test case processing.

ABSTRACT

The Jet Propulsion Laboratory (JPL) has investigated techniques for integrating meteorological data from various satellite sensors to yield a global measure of sea surface wind speed and direction for input to the Navy's operational weather forecast models. The sensors of interest are ones that have been launched or for which firm plans for launch exist, specifically the GOES visible and infrared imaging sensor, the Nimbus-7 SMMR, and the DMSP SSM/I instrument. Several sources of ancillary data were employed.

An algorithm for the extrapolation to the sea surface of wind directions as derived from successive GOES cloud images has been developed. This wind veering algorithm is relatively simple computationally, accounts for the major physical variables, and seems to represent the best solution that can be found with existing data. An algorithm for the interpolation of the scattered observed data to a common geographical grid has been implemented. The algorithm is based on a combination of inverse distance weighting and trend surface fitting, and is well suited to the problems of combining wind data from disparate sources.

Nine meteorological test cases for the Atlantic and Pacific were ultimately selected, for which either NOAA/NESS or SPADS cloud-tracked winds were available. A complete software package was written for their analysis. The original project plan was to apply the interpolation and veering algorithms to the sea surface temperatures and cloud-tracked winds to obtain surface wind direction, then to integrate this result with interpolated surface wind speeds derived from the NIMBUS-7 SMMR instrument. Unfortunately, fairly late in the project it became apparent that the Nimbus-7 wind speed data would not be available. Thus, the complete wind vectors derived from GOES and Nimbus could not be examined. However, this had no substantive effect on the thrust of the project, because the surface wind speed is not an element of the veering computation. The groundwork has indeed been laid for successful integration of the two data types.

The keystone element, the wind veering algorithm, is functioning properly and will provide a firm basis for the integration of cloud-derived wind directions with microwave-derived wind speeds. The software is in place for integrating the wind speeds from Nimbus-7 SMMR or other satellite sensors of opportunity at such a time as the data become available.

TABLE OF CONTENTS

Figures

TABLE OF CONTENTS (Continued)

TABLE OF CONTENTS (Continued)

Tables

DEFINITION OF ABBREVIATIONS

DMSP	Defense Meteorological Satellite Program
FNOC	Fleet Numerical Oceanography Center
GBF	Global Band Fields
GFP	Government Furnished Property
GOASEX	Gulf of Alaska Seasat Experiment
GOES	Geostationary Operational Environmental Satellite
ITCZ	Intertropical Convergence Zone
JASIN	Joint Air-Sea Interaction Experiment
McIDAS	Man-computer Interactive Data Access System
NEPRF	Naval Environmental Prediction Research Facility
NESS	National Environmental Satellite Service--now NESDIS: National Environmental Satellite, Data, and Information Services
PBL	Planetary Boundary Layer
SMMR	Scanning Multichannel Microwave Radiometer
SPADS	Satellite Data Processing and Display System
SSM/I	Special Sensor Microwave/Imager
SST	Sea Surface Temperature
VISSR	Visible and Infrared Spin Scan Radiometer

SECTION 1

INTRODUCTION

Sea surface wind data are sparse over much of the world's oceans. Such data are typically collected by ships and buoys and are largely restricted to shipping lanes. The Fleet Numerical Oceanography Center (FNOC) desires to introduce remote sensing data from satellites into their operational weather models to fill in gaps in worldwide coverage. The purpose of this project is to evaluate techniques that can be used for deriving sea surface wind speed and direction from specific satellite sensors and that can be integrated with existing FNOC computer codes.

This project focuses on satellite sensors both now in orbit and planned for launch in 1985. These are the Geostationary Operational Environmental Satellite (GOES) Visible and Infrared Spin Scan Radiometer (VISSR), the Nimbus-7 Scanning Multichannel Microwave Radiometer (SMMR), and the scheduled Defense Meteorological Satellite Program (DMSP) Special Sensor Microwave/Imager (SSM/I). Successive GOES images can provide wind speed and direction at the cloud level. The SMMR and SSM/I sensors measure wind speed, but not direction, at the sea surface. There are currently no firm plans to launch a scatterometer sensor, which would measure both wind speed and direction at the sea surface, prior to NROSS in 1988.

The overall goal of the project is to determine how to integrate the GOES cloud-tracked winds with the SSM/I winds in an optimal manner to yield sea surface wind speed and direction. Ancillary data are the NEPRF Satellite Data Processing and Display System (SPADS) cloud-tracked winds and the FNOC Global Band Wind Fields (GBF) and Sea Surface Temperature (SST) data. Nimbus-7 SMMR data were to have been GFP (Government Furnished Property) from FNOC as a proxy for future SSM/I data. Because of problems with the Goddard-supplied SMMR wind speed algorithm being used by FNOC, SMMR winds could not be made available for this study. However, this had no substantive effect on the results of the project, because surface wind speed is not an element of the wind veering computation.

The problem of extrapolating the wind at the cloud height to the sea surface is addressed in Section 2. Section 3 describes the procedures used to interpolate the diverse data to a common grid. Section 4 describes the test case selection, and in Section 5 the software is discussed. The test case processing procedures are examined in Section 6, and the meteorological interpretation is discussed in Section 7. Conclusions and references follow.

SECTION 2

WIND VEERING IN THE PLANETARY BOUNDARY LAYER OVER THE OCEAN

The purpose of this phase of the project was to determine the best existing method for the extrapolation of GOES cloud-tracked winds to the sea surface level. Because of the Ekman spiral of wind direction with height, wind direction derived from successive GOES cloud images must be modified to render it applicable to conditions at the sea surface. This is a necessary step in integrating cloud-tracked wind data with ocean surface data.

In 1905, Ekman published the theory for a wind-driven current in an infinite ocean and derived the famous Ekman spiral of velocity with depth. Others extended this theory to the atmosphere. In 1916, Taylor showed theoretically that the lowest layer (~10-20 m in height) of the atmosphere should be a region of constant stress and wind direction, while the next lowest ("Ekman") layer (from ~10-20 m to ~1-2 km) should be a region of decreasing stress and spiraling of the wind direction. The change of wind direction with height is called "veering" and is measured as:

$$\text{veering (deg)} = (\text{wind direction at top of Ekman layer}) - (\text{wind direction at bottom of Ekman layer}) \quad (1)$$

"Positive" veering is defined as clockwise rotation of wind direction with increasing altitude, regardless of hemisphere. Theoretically, there will be positive veering in the Northern hemisphere and negative veering (called "backing") in the Southern hemisphere. Classical Ekman theory predicts veering $\approx 45^{\circ}$, with some modification for latitude. The bulk of the veering occurs in the lowest kilometer of the atmosphere; however, some may also be found in the next lowest kilometer. Over the oceans, the top of the boundary layer is observed to be close to the cumulus base. Observations of wind veering in the Ekman layer were rare prior to World War II but increased thereafter (see references in Mendenhall, 1967; Gray, 1972). The observations rarely agree with classical Ekman theory. Reasons for this may be grouped into two classes, comprising large and small-scale effects. Large-scale effects are vertical stratification and stability, horizontal temperature gradients and advection, the relation of veering to wind speed, and humidity effects. Small-scale effects take the form of random, short-term eddy fluctuations whose magnitudes are large compared to the average veering.

Observed wind veering at any station is highly variable from one observation to the next, with no degree of constancy. Figure 1 shows sample 6-hourly and 12-hourly rawin soundings. These are observed differences between the wind at 1 km and at the surface. Instrumental errors are much less than the observed fluctuations.

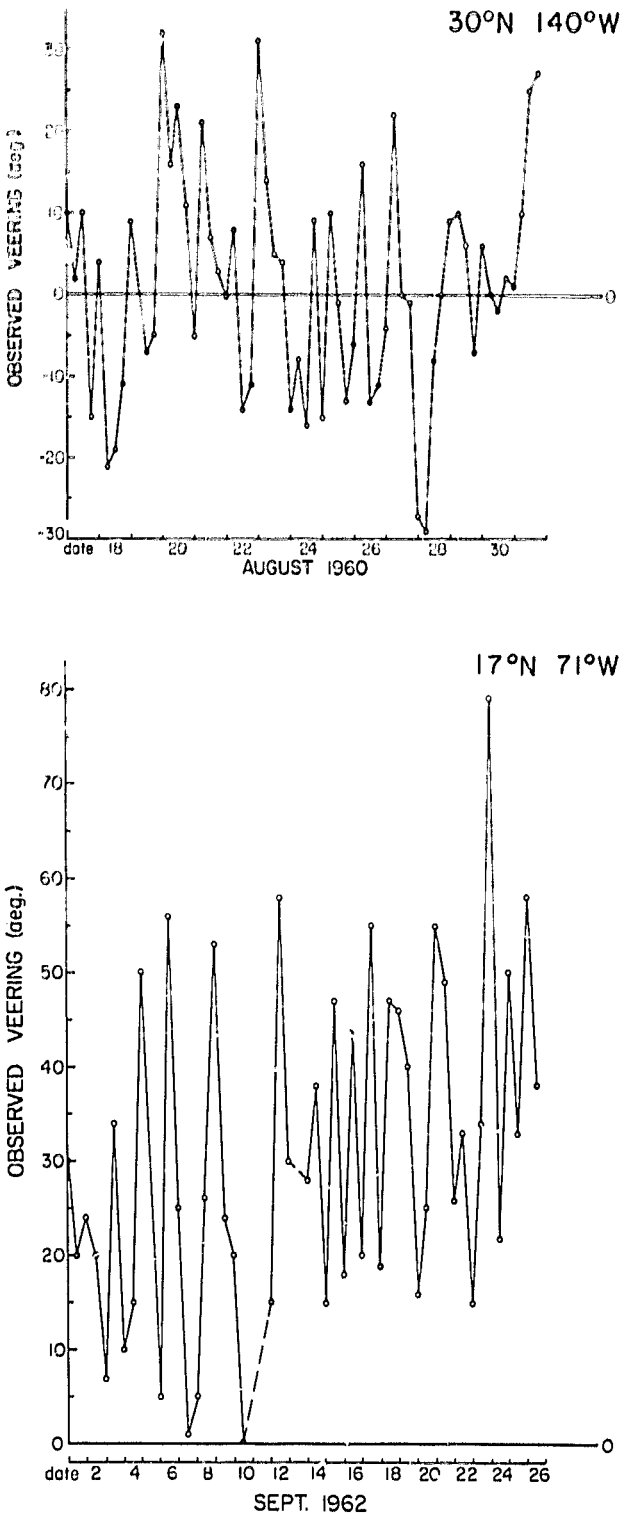

Figure 1. Sample rawin soundings (after Mendenhall, 1967)

2.1 EMPIRICAL STUDIES

Mendenhall (1967) studied veering at two islands and three ships, scattered over the Northern hemisphere. He used rawinsonde observations to give a time base of sufficient length to average out random effects of turbulent eddies and instrumental errors (see Fig. 1). He found that veering decreases in cold advection and thermal instability. He found an average "frictional veering" (i.e., after deviations from the average due to advection, stability, etc., are removed) of 10°. Other authors often use a mean veering angle of 10° or 15° (e.g., Willebrand, 1978) when modeling the PBL.

Gray (1972) performed the only hemisphere-wide statistical study. Over 100,000 pibal and rawin observations over the oceans from 1949 to 1964 were analyzed, for latitudes 0° - 60°N. He found that the thermal wind, which takes the form of cold and warm air advection, has a very pronounced effect on veering, while vertical stability (lapse rate) has very little effect on veering. He also found average relationships between veering and latitude, wind speed, and season. Figure 2 shows the relation between veering and direction as a function of latitude.

North and south wind differences are interpreted in terms of thermal wind differences for cold and warm air advection, respectively. On the average, in the Northern hemisphere, northerly winds are cold and will advect cold air over warm water, creating an unstable condition. Intuitively, one would expect greater vertical coupling in an unstable PBL and less veering, which is seen. On the average, southerly winds in the Northern hemisphere are warm and will advect warm air over cold water, leading to a stable condition with more veering. Easterly and westerly winds are intermediate cases. Figure 3a shows the average veering - wind speed relation. Figure 3b shows the average veering - season relation.

Together, these data present a nice, simple picture of the average veering, and it is tempting to use them as a solution. However, although these results are often close to actual veering, they often do not hold in specific cases. This is mainly because northerlies are not always cold and southerlies are not always warm. Actual local advection conditions must be taken into account. Indeed, Gray (1982) suggests the use of an average veering of 10°, modified according to advection.

Before describing the semiempirical equation that appears to be the best solution to the veering problem, other empirical studies will be briefly discussed. Because their geographical areas (Figure 4) all cross the equator, special problems in that region should be mentioned. Within about 10° to 15° of the equator, there exists a different kind of meteorology. The Coriolis force becomes very weak and geostrophy breaks down. It is replaced by cyclostrophy, a balance between the pressure force and the centrifugal force due to curvature. The pressure gradient is weak and the streamlines wander or meander. Predictive techniques break down in this region. Most investigators avoid this area when testing out models. The winds at 500 mb in this region can be 180° from the surface winds (Sadler, 1982; Chelton, 1982a).

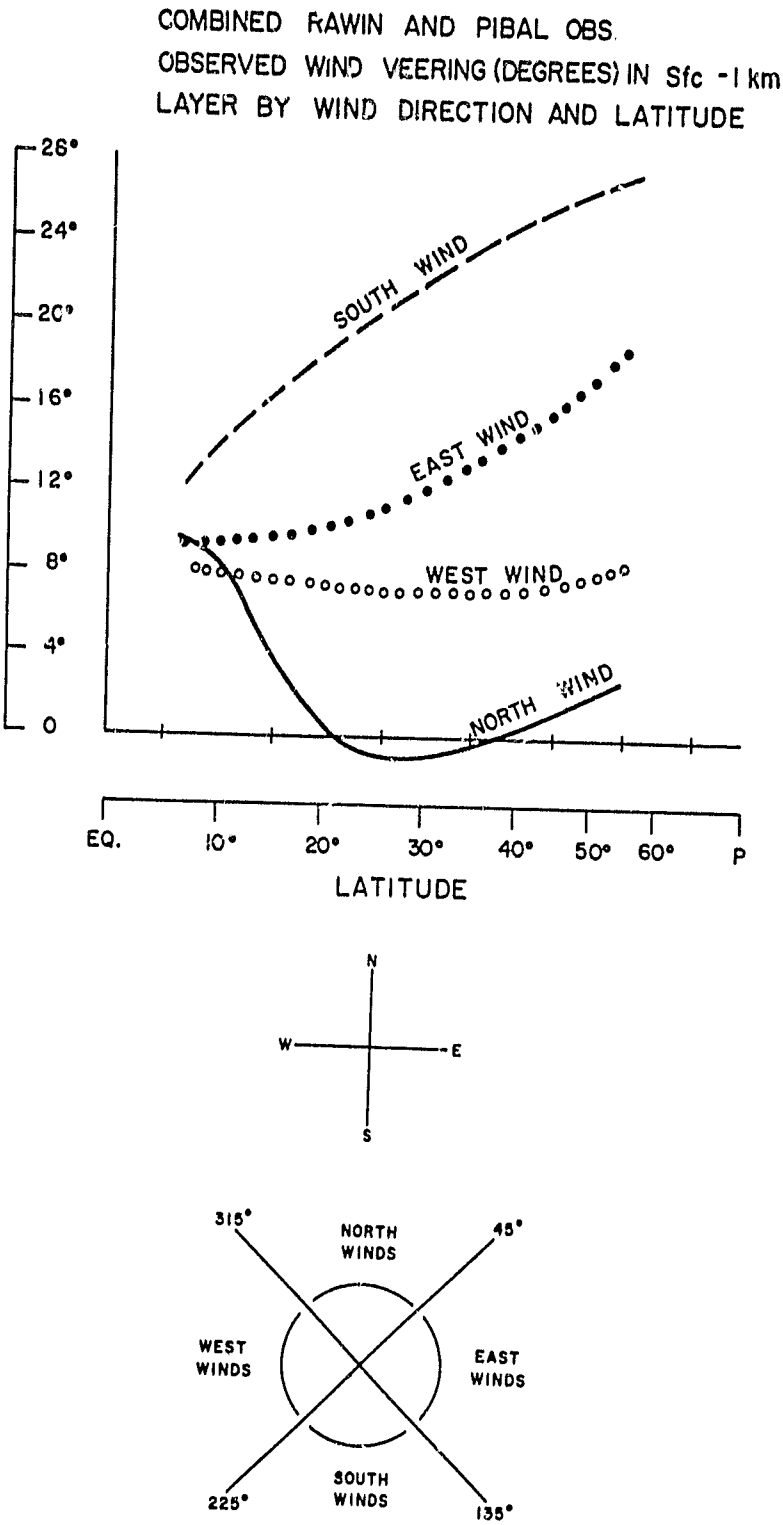

Figure 2. Veering stratified by direction and latitude (after Gray, 1972)

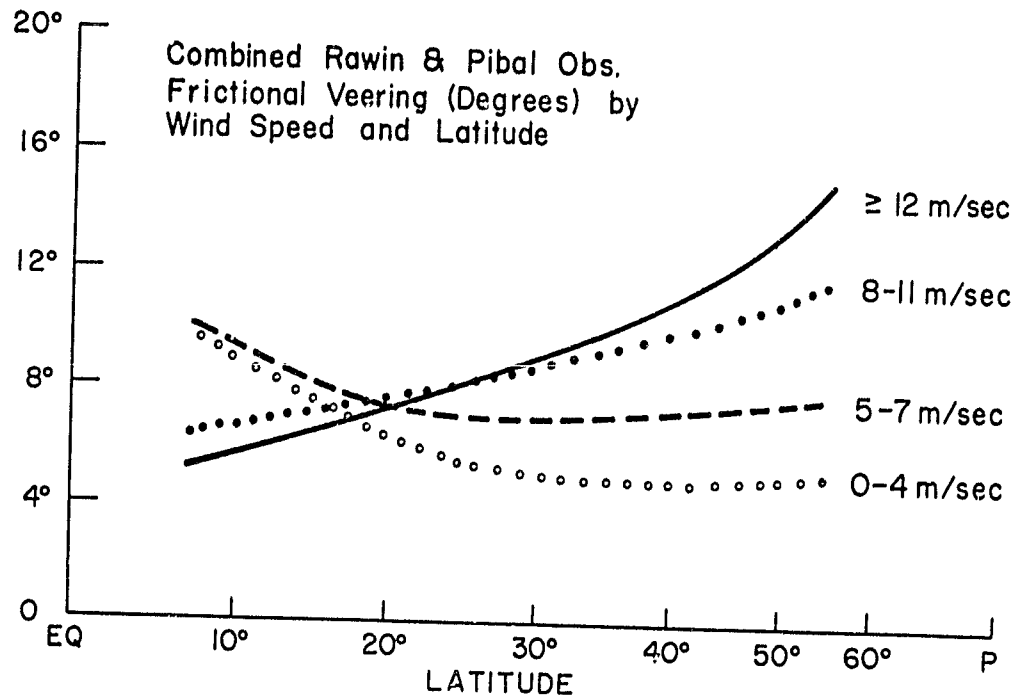

Figure 3a. Latitude distribution of frictional veering by wind speed (after Gray, 1972)

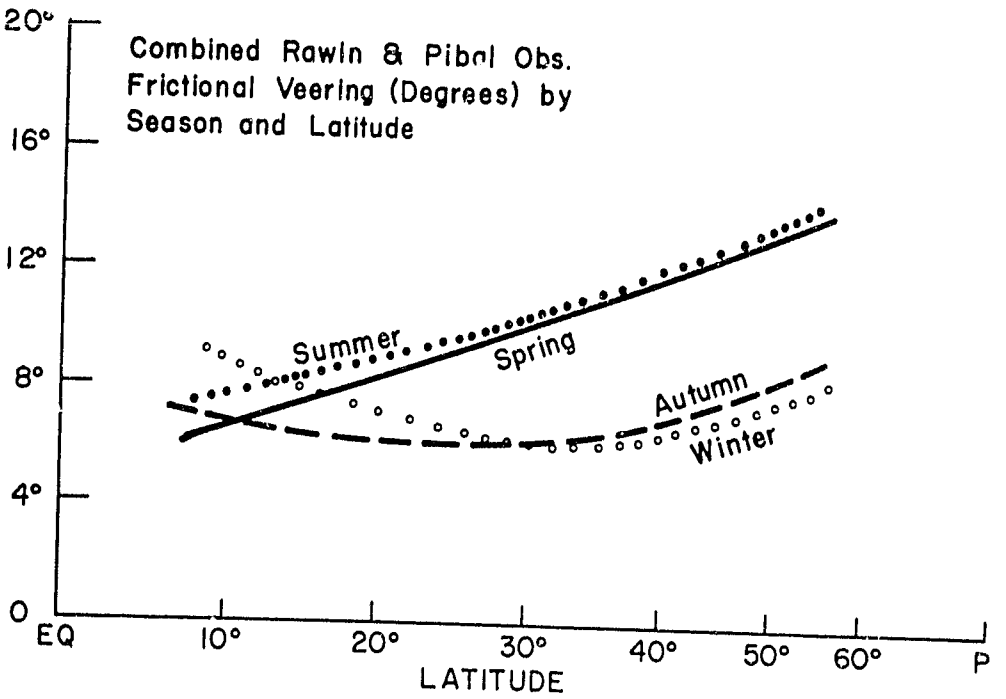

Figure 3b. Frictional veering by latitude and season (after Gray, 1972)

In all of the empirical studies discussed below, cloud winds, rather than pibal and rawin soundings, were compared to surface winds. Wylie and Hinton (1981, 1982b) studied veering for a one-year period over the Indian ocean (area indicated in Figure 4) using GOES McIDAS winds and ship data totaling several thousand pairs. Results were stratified according to geographical location, wind speed, wind direction, and season. Exclusive of speed, the results are shown in Figure 5. (Wylie (1982) notes that the Arabian Sea, Bay of Bengal, and Southern midlatitude results should not be relied upon in detail.)

Of special interest is the northerly wind (arrow pointing south) in the Arabian Sea, which is hot in the summer (high veering) and cool in the winter (low veering). In general, there is veering in the Northern hemisphere and backing in the Southern hemisphere, as would be expected. Many of the southerlies just north of the equator exhibit backing, indicating a memory effect as pointed out by Mahrt (1972). The authors find less veering with increasing wind speed, in agreement with Gray (1972) for latitudes below $\sim 20^{\circ}$.

Schott and Fernandez-Partagas (1981) studied a subset of this area, the Somali coast, during March - July, 1979. They found small amounts of veering, increasing with latitude and showing some memory effect across the equator (Figure 6).

Enfield (1981) studied the veering between GOES IR clouds and surface streamlines over the Southeast Tropical Pacific (Figure 4) for the period 1974 - 1980. On the average, there was backing in the Southern hemisphere with a range of 0° - 20°. He found increased veering toward the equator, which conflicts with Gray (1972). He also found systematic seasonal variations, which are most likely caused by changing advection conditions.

Halpern (1979, 1980) and Halpern and Knox (1982) studied veering over three very small areas (Figure 4) of the central Pacific near the equator, using GOES winds and buoys, over periods of a few months. They found veering of northeasterly winds, backing for southeasterly winds, and zero veering for easterly winds. The mean values were veering $\sim 34^{\circ}$ and backing $\sim 30^{\circ}$ - 35°, which do not agree with Gray (1972) or the proposed algorithm in Section 2.4 of this paper. This points out the problems associated with latitudes within 10° of the equator.

Sadler and Kilonsky (1981, 1981b) constructed monthly long-term averages of 7 years of NESS satellite winds over the Pacific (Figure 4). They also constructed monthly long-term averages of ~ 30 years of ship winds. Averaged over one month, the two are significantly correlated and coherent (without correction for veering). Correlation disappears for averaging periods smaller than 15 days (Sadler, 1982). Subtraction of the two long-term averages gives the climatological veering (e.g., Figure 7; Sadler, 1982). For a specific month of satellite observations, this climatological veering is subtracted out to derive the surface winds from satellite winds. This method outperformed five other methods at a 1980 Seattle workshop (Sadler, 1982). However, such climatological averaging is dangerous because it will not be good for unusual conditions, e.g., an unstable PBL.

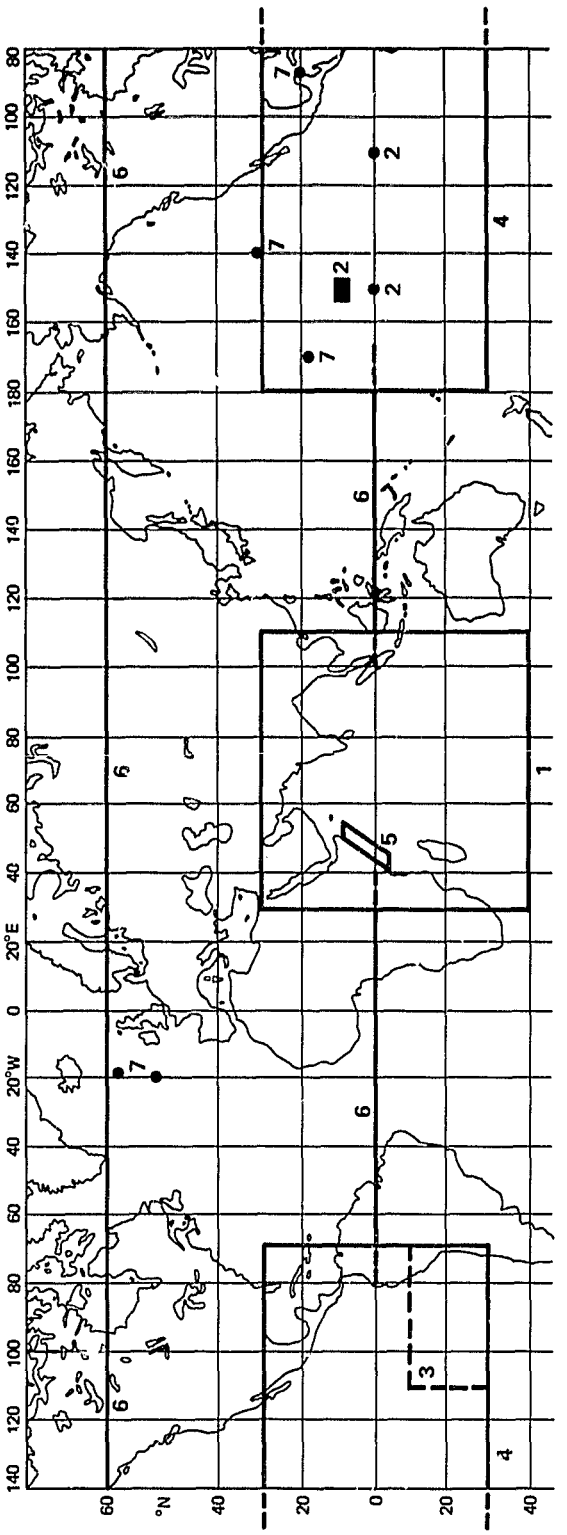

Figure 4. Geographical distribution of empirical studies

1. Wylie and Hinton (1981, 1982)
2. Halpern (1979, 1980); Halpern and Knox (1982)
3. Enfield (1981)
4. Sadler and Kilonsky (1981 a, b)
5. Schott and Fernandez-Partagas (1981)
6. Gray (1972)
7. Mendenhall (1967)

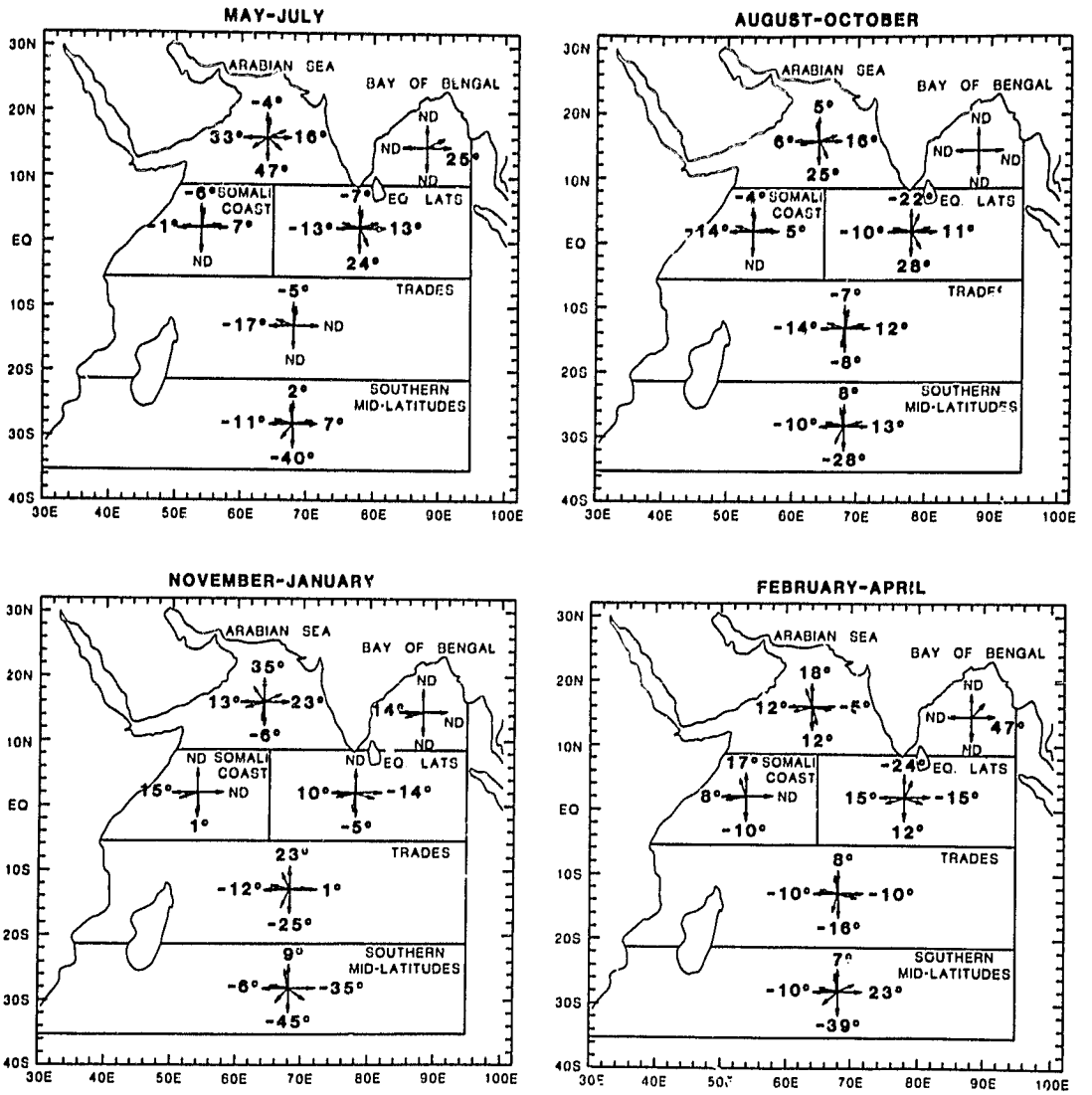

Figure 5. Mean sub-cloud wind directional veering for each season and geographical area (all wind speeds averaged together). The cloud - ship comparisons were stratified according to 4 quadrants based on the cloud motion direction. A positive angle indicates an average veering between the cloud and ship levels, cloud direction greater than ship direction. (After Wylie and Hinton, 1982b.)

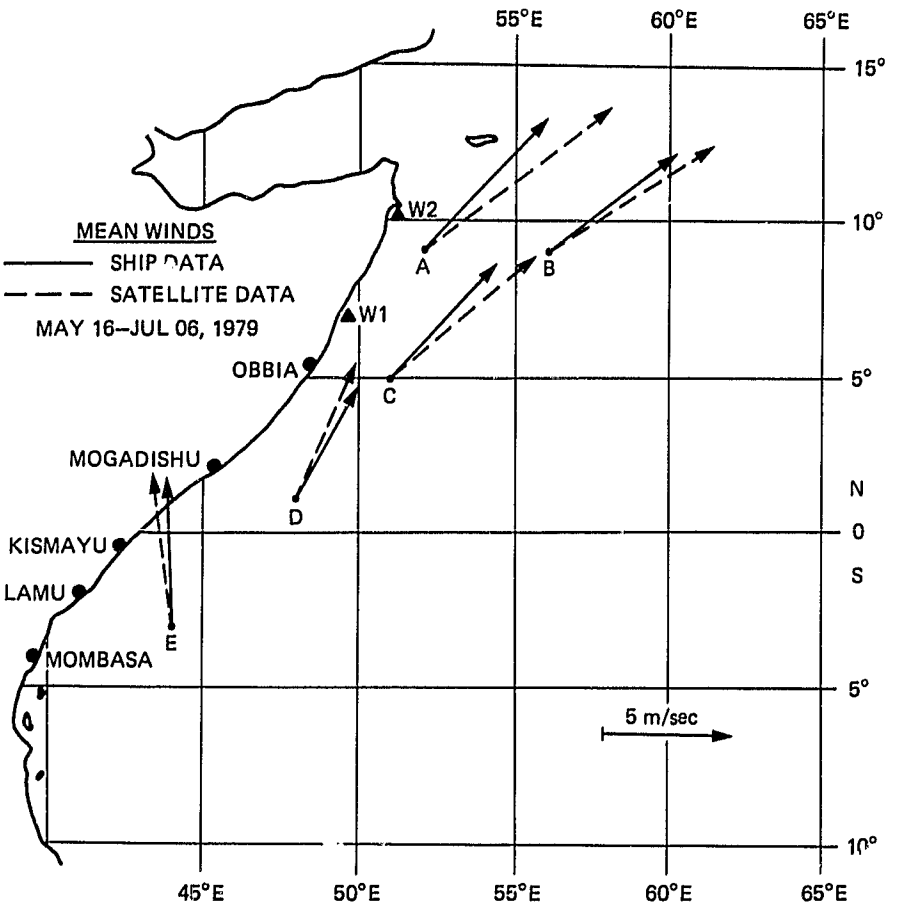

Figure 6. Veering along the Somali coast (After Schott and Fernandez-Partagas, 1981)

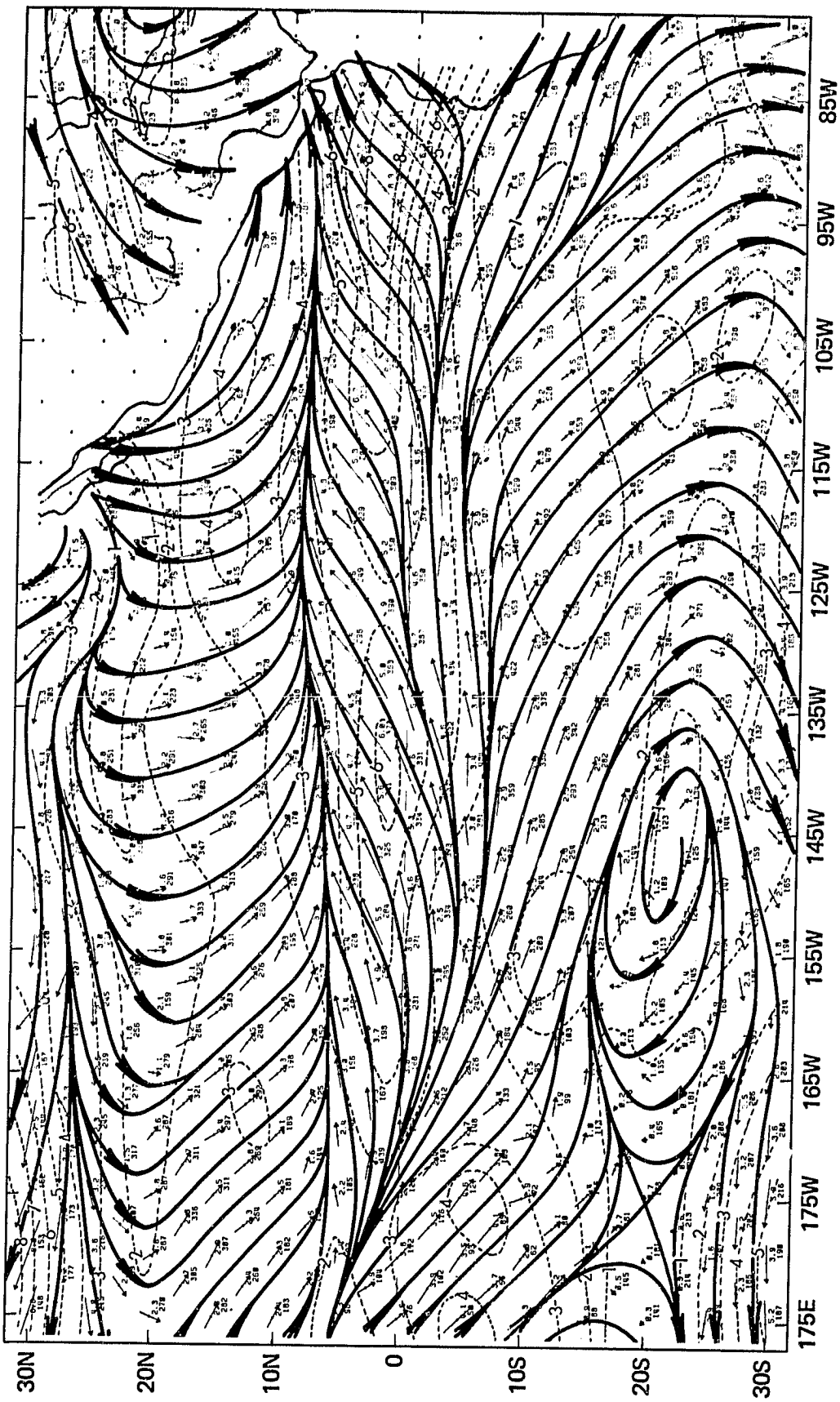

Figure 7. December monthly mean shear between ship winds and low-level sawins. Period of data: ships 1947-1978; sawins 1974-1981. Speed in m/sec. (After Sadler, 1984.)

The global coverage of these data is incomplete; they include the troublesome tropical region. Comparison of these results with the proposed algorithm in Section 2.4 might be possible, given climatological SST data.

2.2 SEMIEMPIRICAL STUDY

Caton et al. (1978) developed equations for the derivation of sea surface winds from the sea-level pressure field. First, the geostrophic wind equation is used to compute the geostrophic wind from the pressure gradient. A trajectory curvature correction is then performed to compute the gradient wind from the geostrophic wind. Empirically based equations are then used to correct the computed gradient wind speed and direction for the effects of the PBL, i.e., slowing and veering. The constants in these equations were calibrated by comparing approximately 30 million (Mendenhall, 1982) ship winds to the theoretical gradient/geostrophic winds. Caton et al. do not state the relation between the gradient wind direction and the observed cloud wind direction. According to Wylie (1982) and Mendenhall (1982) the two are essentially the same. Given this, the equation for veering will correctly bring cloud wind directions down to the surface. The equation is:

$$\theta^{o}_{clouds} - \theta^{o}_{surface} = 10^{o} + 10^{o} \sin\left[\frac{\pi}{2} \times 2470 \times (\underline{V}gr \cdot \nabla T)\right] + 0.5^{o}T \quad (2)$$

where 10^{o} is the average veering which is modified by advection in the form of the scalar product $\underline{V}gr \cdot \nabla T$, where $\underline{V}gr$ is the gradient wind vector and T is the sea surface temperature (SST). This assumes that air temperature and its gradient mimic sea surface temperature and its gradient, which is a reasonable assumption (Wylie, 1982; Gray, 1982). Use of this scalar product is quite conservative, whereas use of a different measure of stability such as the air-sea temperature difference is often of questionable accuracy. Note that the veering variation with wind speed is incorporated implicitly into this equation, and that $\underline{V}gr$ points in the direction that the wind is coming from. The SST gradient should be taken over 3^{o} - 5^{o}. The last term in the equation is supposed to be an empirical correction for latitude.

This equation produced numbers that vary from 0^{o} for maximum cold advection at $T = 0^{o}C$ to a possible 35^{o} for maximum warm advection at $T = 30^{o}C$. The absolute magnitude of the advection, $\underline{V}gr \cdot \nabla T$ is limited to $\leq 4 \times 10^{-4}{}^{o}C/sec$. The equation should be as good as Gray's average veering in cases where his method is good, and it should be much better in cases where his method fails, because it takes into account actual advection conditions. It appears to be the best solution to the veering problem.

However, the empirical correction for latitude in this equation is not satisfying because it assumes a one-to-one correlation between latitude and SST. Mendenhall (1982), as a result of conversations regarding this project, devised a theoretically based term as a replacement. This term would replace both the 10^{o} average veering and the $0.5^{o}T$ term.

Comparison of the numerical values of this replacement term with the observed data revealed that it is not a satisfying solution, either. The computed veering variation with latitude is much stronger than the observed (e.g., Gray, 1972) variation, and it is of the wrong sign. Further conversations (Mendenhall, 1982; Gray, 1982) failed to provide a solution. As a result, a latitudinal term based on synthesis of the observed data has been chosen. It is $0.12^{\circ}\ |\phi|$, where $|\phi|$ is the absolute value of the latitude in degrees. Then the equation is:

$$\theta^{\circ}_{clouds} - \theta^{\circ}_{surface} = 10^{\circ} + 10^{\circ} \sin\left[\frac{\pi}{2} \times 2470 \times (\underline{V}gr \cdot \nabla T)\right] + 0.12^{\circ}|\phi| \qquad (3)$$

On the average, veering increases with latitude. There are more complicated secondary effects with inflection points at $\sim 20^{\circ}$. These probably give rise to reports by some investigators that veering decreases with latitude in the tropics.

This equation produces numbers that vary from about $0^{\circ} - 20^{\circ}$ near the equator to $8^{\circ} - 28^{\circ}$ at $\phi = 67^{\circ}$. This is in reasonable agreement with other data in Gray (1972), although there is some indication that the advection term should be made more dominant with respect to the latitudinal term.

This equation does not apply within 10° of the equator. As noted in Section 2.1, there are special problems in this region. A solution for this region is proposed in Section 2.4.

2.3 THEORETICAL STUDIES

Numerous theoretical studies of the planetary boundary layer have been made in the past, alternatively concluding that veering should increase or decrease toward the equator and indicating the importance of stability (e.g., Clarke and Hess, 1975; Mahrt, 1972). The state of the art in theoretical models of the PBL is represented by Brown and Liu (1982). Like Caton et al. (1978), they start with the sea-level pressure field, compute the geostrophic wind, then correct for isobar curvature to derive the gradient wind. This geostrophic/gradient wind is assumed to be at the top of the PBL. At this point, rather than use a semiempirical equation for veering, they use a detailed PBL model. The required inputs to the model are the air-sea temperature difference, the synoptic-scale air temperature fields, and the humidity. The model was tested against measurements made during the GOASEX and JASIN experiments, and usually was able to predict veering to within 20° or better. Average veering for unstable stratification was $0^{\circ} - 10^{\circ}$, and for stable stratification was $\sim 25^{\circ}$; the veering increases with wind speed (Brown, 1982). The model has not been tested in the tropics.

There are two drawbacks to the model. One is that most of the required input data are normally unavailable. Without humidity and precise air-sea temperature differences, the model will not perform (Liu, 1982). The other is that the model is overly complicated with respect to the goal of finding a simple veering algorithm, and, as most of the consulted experts agreed,

would not add much to the semiempirical formulation. Hence, a theoretical PBL model is not felt to be an acceptable solution to the problem.

2.4 THE PROPOSED ALGORITHM

2.4.1 Latitudes 10° and Above

As noted in Section 2.1, geostrophy breaks down within 10° to 15° of the equator. Thus the thermal wind in the form of the advection term is no longer valid. (Gray (1982) suggests that advection is still important at 15° but not at 10°). For all latitudes outside of this range the proposed algorithm is

$$\theta^{\circ}_{clouds} - \theta^{\circ}_{surface} = \pm 1 \left\{ 10^{\circ} + 10^{\circ} \sin \left[\frac{\pi}{2} \times 2470 \times (\underline{V}gr \cdot \nabla T) \right] + 0.12^{\circ} |\phi| \right\} \quad (4)$$

where

$|\phi|$ = absolute value of ϕ
$+1$ holds for $\phi > +10^{\circ}$
-1 holds for $\phi < -10^{\circ}$

This is the same as Equation 3 except for the ± 1 term, which is used to differentiate between hemispheres. Veering is negative ("backing") in the Southern hemisphere.

2.4.2 Latitudes 0° to 10°

One possible solution in this region would be to hold the magnitude of the average veering at $\phi = 10^{\circ}$ constant across the equator. This magnitude would be veering = $10^{\circ} + 0.12\ \phi = 9.7^{\circ} \approx 10^{\circ}$. The sign change at the equator would result in a large discontinuity. The proposed solution is to reject Equation 4 in this region and to use Gray's average results for these latitudes. His results for veering from the surface to 1 km and from 1 km to 2 km were summed, and the results were scaled by $\approx 1{:}5^{\circ}$ so that they would blend smoothly into the 9.7° average value at $\phi = 10^{\circ}$, as predicted by the advectionless equation. The numbers so derived are listed in Table 1.

Table 1. Veering for $|\phi| \leq 10^{\circ}$

(DEGREES)	VEERING (DEGREES)
± 10.0	± 9.7
7.5	8.2
5.0	6.7
2.5	5.0
0.0	0.0

2.4.3 Assumptions

The assumptions that went into the proposed algorithm are listed below:

(1) The gradient wind direction is the same as the observed cloud wind direction.

(2) The air temperature gradient mimics the sea surface temperature gradient.

(3) The overall variation of veering with latitude derived from pibal and rawin observations is of the same form as that which would be derived from satellite observations.

(4) The magnitude of the advection term will never be greater than 4×10^{-4}°C/sec (i.e., $|\underline{V}gr[cm/sec] \cdot \nabla T[^{\circ}C/cm]| \leq 4 \times 10^{-4}$).

(5) Gray's (1972) results are representative of the average veering within 10° of the equator.

2.4.4 Data Requirements

The proposed algorithm requires the following input data:

(1) The satellite wind direction and magnitude derived from cloud-tracking methods.

(2) The sea surface temperature gradient direction and magnitude, taken over a distance of 3° to 5°.

(3) Latitude.

2.4.5 Second-order Effects

Second-order effects that will complicate the veering problem are listed below:

(1) Vertical stability (lapse rate).

(2) Hot or cold winds off land masses, in which temperatures are not reflected in the SST.

(3) Crossover point at $\phi \sim 20^{\circ}$ in the veering - wind speed relation.

(4) Possibly nonlinear general latitude relation.

(5) Humidity.

(6) Breakdown of geostrophy at $|\phi| < 10^{\circ}$ (actually a primary effect).

(7) Memory effect across the equator.

2.4.6 Future Work

Future investigation of the veering problem could potentially include the following topics:

(1) Search for a better solution at $|\phi| < 10^{o}$, perhaps a climatological average veering similar to the work of Sadler, extended over all longitudes.

(2) Investigate the incorporation of some of the second-order effects listed above.

(3) Study the effect of replacing temporal averaging with spatial averaging.

2.5 PERSONS CONSULTED ON WIND VEERING

Don Wylie	University of Wisconsin
Bruce Mendenhall	Science Applications, Inc.
Jim Sadler	University of Hawaii
Dave Halpern	Pacific Marine Environmental Laboratory
Bill Gray	Colorado State University
Manfred Holl	Meteorology International, Inc.
Bob Brown	University of Washington
Tim Liu	Jet Propulsion Laboratory
Bob Knox	Scripps Institute of Oceanography
T. Krishnamurti	Florida State University
Walter Munk	Scripps Institute of Oceanography
Dudley Chelton	Jet Propulsion Laboratory
G. T. Kaye	Naval Ocean Systems Center
Bob Stewart	Jet Propulsion Laboratory Scripps Institute of Oceanography
Steve Pazan	Jet Propulsion Laboratory Scripps Institute of Oceanography
David Enfield	Oregon State University

SECTION 3

OBJECTIVE ANALYSIS

The purpose of this phase of the project was to determine the objective analysis procedures to be utilized in analyzing the data. Geophysical data are normally analyzed on a regularly spaced grid of points, to afford ease of comparison, interpretation, numerical analysis, and plotting. Real data are not, however, acquired on a regular grid. The process whereby data at the grid points are interpolated from the observed data is known as objective analysis. Use of the word "objective" means that the interpolation procedure can be quantified mathematically.

3.1 ENDLICH-MANCUSO OBJECTIVE ANALYSIS TECHNIQUE

The Endlich-Mancuso method of objective analysis (Endlich and Mancuso, 1968) is a combination of Shepard's method of inverse distance weighting and of trend surface fitting. The method meets the general requirements for objective analysis of the data to be analyzed in this project. It is a relatively simple method which is easy to implement. At each grid point, typically the five nearest observations of some scalar field T are identified. A first degree polynomial of the form

$$T_p(x,y) = \beta_o + \beta_1 x + \beta_2 y$$

is fit to these two-dimensional data. Such a dipping flat plane will smooth the data since it does not fit the observations exactly. The coefficients β_i are found by minimizing the sum of square errors at the five observation points. If T_i is the observed scalar quantity and T_p is its polynominal estimate, a trend surface would be fit by minimizing

$$\sum_{i=1}^{n} (T_i - T_p)^2$$

or (5a)

$$\sum_{i=1}^{n} (T_i - \beta_o - \beta_1 x_i - \beta_2 y_i)^2$$

This quantity is minimized by differentiating with respect to the β_i and setting the resulting equations equal to zero.

Endlich and Mancuso improve on this method by introducing an inverse-square distance weighting factor W for each observation. This factor reduces the amount of smoothing created by the trend surface fit when the five observations are spread over a large area. It also makes the analyzed grid point values agree more closely with nearby observations. The weighting factor is given by

$$W_i = \frac{C^2}{R_i^2 + R_i^{*2} + C^2} \qquad (5b)$$

where C^2 = constant = 6 for upper air analysis and 3 for surface analysis, subjectively chosen to make the smoothing comparable to hand analysis; R = distance from the grid point to the observed point, in degrees of arc. As a good approximation (Chelton, 1982a),

$$R = \left[\Delta x^2 + \Delta y^2\right]^{1/2}$$

$$= \left[\left\{\left|lon_1 - lon_2\right| * \cos\frac{1}{2}(lat_1 + lat_2)\right\}^2 + (lat_1 - lat_2)^2\right]^{1/2}$$

R^* varies from 0 to R, and measures the direction or heading of the observed point from the grid point.

$$R^* = \left|\frac{\underline{k} \cdot \underline{R} \times \underline{V}}{|\underline{V}|}\right|$$

$$= \frac{RV\sin\theta}{V}$$

$$= R\sin\theta$$

where θ is the angle between $\underline{R}$ and $\underline{V}$, as shown in Figure 8.

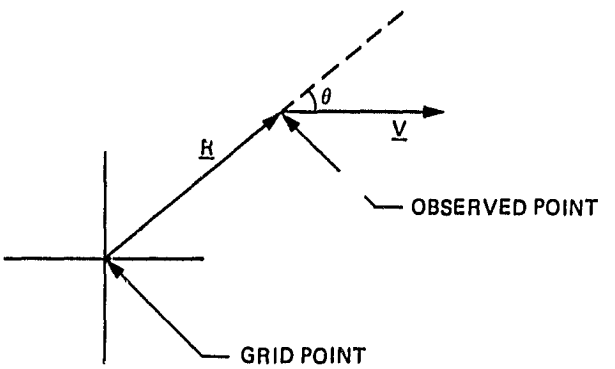

Figure 8. Elliptical weighting

If the observed point is in an upwind-downwind direction from the grid point, $\theta = 0^\circ$ and $R^* = 0$, giving maximum weighting. If the point is in a crosswind direction, $\theta = 90^\circ$ and $R^* = R$, giving minimum weighting. This is called elliptical weighting because of its shape. Its physical relevance lies in the fact that upwind-downwind length scales are greater than crosswind length scales.

The introduction of this weighting factor into Equation 5 means that the quantity to be minimized is

$$\sum_{i=1}^{5} W_i(T_i - T_p)^2$$

or (6)

$$\sum_{i=1}^{5} W_i(T_1 - \beta_o - \beta_1 x_i - \beta_2 y_i)^2$$

To solve this problem, differentiate with respect to the β_i and set the resulting equations equal to zero:

$$-2\sum_{i=1}^{5} W_i(T_i - \beta_o - \beta_1 x_i - \beta_2 y_i) = 0$$

$$-2\sum_{i=1}^{5} W_i x_i(T_i - \beta_o - \beta_1 x_i - \beta_2 y_i) = 0$$

$$-2\sum_{i=1}^{5} W_i y_i(T_i - \beta_o - \beta_1 x_i - \beta_2 y_i) = 0$$

This is a weighted multiple regression problem which can be solved on the computer by standard matrix techniques. The solution (Pihos, 1982) is

$$\Delta \equiv \begin{vmatrix} \Sigma W_i & \Sigma W_i x_i & \Sigma W_i y_i \\ \Sigma W_i x_i & \Sigma W_i x_i^2 & \Sigma W_i x_i y_i \\ \Sigma W_i y_i & \Sigma W_i x_i y_i & \Sigma W_i y_i^2 \end{vmatrix}$$

$$\beta_o = \frac{1}{\Delta} \begin{vmatrix} \Sigma W_i T_i & \Sigma W_i x_i & \Sigma W_i y_i \\ \Sigma W_i x_i T_i & \Sigma W_i x_i^2 & \Sigma W_i x_i y_i \\ \Sigma W_i y_i T_i & \Sigma W_i x_i y_i & \Sigma W_i x_i y^2 \end{vmatrix}$$

$$\beta_1 = \frac{1}{\Delta} \begin{vmatrix} \Sigma W_i & \Sigma W_i T_i & \Sigma W_i y_i \\ \Sigma W_i x_i & \Sigma W_i x_i T_i & \Sigma W_i x_i y_i \\ \Sigma W_i y_i & \Sigma W_i y_i T_i & \Sigma W_i y_i^2 \end{vmatrix}$$

$$\beta_2 = \frac{1}{\Delta} \begin{vmatrix} \Sigma W_i & \Sigma W_i y_i & \Sigma W_i T_i \\ \Sigma W_i x_i & \Sigma W_i x_i^2 & \Sigma W_i x_i T_i \\ \Sigma W_i y_i & \Sigma W_i x_i y_i & \Sigma W_i y_i T_i \end{vmatrix}$$

where $|\ |$ is the determinant of a matrix and Σ indicates the sum from $i = 1$ to 5.

Given the β_i, the value of T at the grid point, defined as T_g, can now be computed by evaluating the polynomial $T_p(x,y)$ at the grid point location x_o, y_o:

$$T_g \equiv T_p(x_o, y_o) = \beta_o + \beta_1 x_o + \beta_2 Y_o$$

Modifications to this technique are made in certain circumstances. If any two of the five observed points are closer together than 30 miles, the next nearest station is included in the analysis, to total six points. In areas of sparse data, the five weighted observed points are averaged, and this value is assigned, with a low weight, to the grid point. This point is treated as a sixth observation.

3.2 APPLICATION OF ENDLICH-MANCUSO

3.2.1 Satellite Winds Gridding

The satellite winds data provide a measure of wind speed and direction at height in the atmosphere. The Endlich-Mancuso scheme is quite suitable to such data. In Equation (5), C^2 is set to 6.

Standard practice (Caton et al., 1978) is to convert the wind vector to its U and V components prior to interpolation. The conversion is

$$U = -S\sin\phi$$
$$V = -S\cos\phi$$

where $\phi = 0^o$ toward the north and increases clockwise and S is wind speed. The standard meteorological convention is that ϕ is in the direction that the wind is coming from.

The number of points to be used in the interpolation has been suggested by Endlich and Mancuso as five. The maximum radius is often chosen to be twice the spacing of the interpolated grid points at the equator (Pazan, 1982). A maximum time cutoff ($\pm 3^h$) should also be employed.

Observed points which lie on the grid points can be handled in one of two ways, at the discretion of the user. One method is to assign those observations to the grid point values, and do no interpolation.

The other method is to perform interpolation, using the observed value at the grid point with a high weight, i.e., $R_i = 0$, $R_i^* = 0$, and $W_i = 1$. (There are no singularities in any of the parameters.) This second approach is the one that was used in test-case processing.

3.2.2 SST Gridding

The Endlich-Mancuso technique is inappropriate for gridding SST data, because it would tend to smear the data and reduce the SST gradient. SST data are gridded using a bilinear interpolation technique. The specifics of this technique are outlined in Section 6.

3.2.3 Global Band Wind Field Gridding

The gridding technique is the same as for satellite winds gridding, except that the wind direction must be computed from the U and V components output from the global band wind field ingestion module. Given the previous definitions, the conversion is

$$\phi = \tan^{-1}\left(\frac{U}{V}\right)$$

This completes the description of gridding the data sets for this project.

3.3 OTHER OBJECTIVE ANALYSIS METHODS

A brief description is given below of other methods that were considered but not used in this project.

3.3.1 Fields by Information Blending (FIB)

The FIB technique (Caton et al., 1978; Mendenhall et al., 1977) is intermediate in sophistication between the Endlich-Mancuso and the optimal interpolation methods. It is a mathematically complex technique that combines diverse information in its estimation of meteorological fields. A first-guess sea-level pressure field is derived by analyzing data from the past two weeks. Current information is then merged with this first-guess field, and points that are grossly wrong are eliminated. A process of "blending" is then performed, which spreads diverse information from a given point to the surrounding grid points by using the gradients and Laplacians of the fields, in an attempt to make a best fit to all of the data by accounting for their spatial variations. The blending process helps to add information to grid points that originally had few observations assigned to them. Next, all the grid point weights are recomputed, bad points are rejected, and the process is iterated back to the step in which the current information is merged.

If an objective analysis technique of such complexity is to be used in practice, it should perhaps be optimal interpolation rather than FIB. The former seems to account better for the physics of the meteorological parameters, without becoming as dependent on formal mathematical analysis.

3.3.2 Optimal Interpolation

The optimal interpolation technique (Gandin, 1965; Chelton, 1982b) uses the spatial covariance function and weights the five closest points in a least-squares sense. This interpolation method allows estimation of the errors in the results, so estimates can be accepted or rejected on the basis of a quality test (Chelton, 1982a). The technique considers the physical attributes of the fields, e.g., the fact that the pressure field is smoother than the wind field, and makes use of the statistical structure of the data. In operation, the observed values at the five points closest to a given grid point are subtracted from their climatological means. A suitably weighted linear combination of these deviations from the mean is used to compute the deviation at the grid point. The weights are computed by requiring that the mean square error be minimized. Unlike the Endlich-Mancuso method, the optimal interpolation method objectively determines the weights. For high data densities, the two methods are of comparable accuracy. For low data densities, optimal interpolation is superior to Endlich-Mancuso (Pazan, 1982). Optimal interpolation is more difficult to use and is generally more expensive than the Endlich-Mancuso technique.

SECTION 4

TEST-CASE SELECTION

The purpose of this phase of the project was to select the locations and times of the data sets to be used in testing and refining the software. The goal of the selection was to represent a wide range of meteorological and physical conditions potentially affecting cloud tracking and sensor performance.

4.1 DATA TYPES AND SOURCES

Table 2 outlines the types of data used in this project and their sources.

Table 2. Data types and sources

Type	Source	Remarks
NOAA/NESS Winds	FNOC	No temperature or pressure data available
SPADS Winds	NEPRF	An independent source of satellite winds
Global Band Fields	FNOC	The standard existing product for surface winds
Sea Surface Temp.	FNOC	Element of the veering computation
GOES Images	NOAA/NEPRF	For vector field display background
(Nimbus-7 SMMR)	-	(Wind speeds unavailable)

4.2 SELECTION CRITERIA

The following selection criteria were used in selecting the NOAA/NESS test sites. As noted in Section 1 SMMR data were originally to have been used in this project. This was still planned long after the site selection phase was complete. Hence, the selection process was restricted by SMMR characteristics. After it was determined that SMMR data would be unavailable for this project, there was no opportunity to choose new cases, with the exception of the four SPADS cases.

Data are to be considered contemporaneous if acquired within a ± 3 hour window. The site areas are restricted to the Western Atlantic and Pacific; there is no available SMMR coverage for the Eastern Atlantic. The site times are restricted to 1981. The SMMR instrument was turned off on even Julian days during 1981 to conserve spacecraft power. SMMR is restricted to ascending orbits only, which corresponds to daylight at the site. The sites are restricted to $\pm 60^{\circ}$ latitude by GOES coverage. The longitudinal extent of the site should be at least 750 km for one SMMR swath and 3000 km for two swaths. Global band and SST data are available for FNOC analysis times of 0000Z and 1200Z only. NOAA/NESS winds are scattered over 24 hours

(restricted to daylight). Not all data types are available for all dates and times. A wide range of meteorological conditions should be chosen.

4.3 SELECTION PROCEDURE

GOES browse images for 1981 were acquired; for GOES-East, a 16-mm movie covering the May-October time period was obtained from NOAA. For GOES-West, hard-copy images were borrowed from Dr. Robert Bornstein at San Jose State University.

Using these images, a total of 65 potential test sites were identified in conjunction with the following experts: a climatologist, Jim Huning; a sensor engineer, Eni Njoku; an oceanographer, Dudley Chelton; a meteorologist, Peter Woiceshyn.

Using NIMBUS-7 orbital elements, SMMR swath maps were processed for the selected dates. The restriction to coincident ascending orbits brought the number of potential test sites to 17. The lack of various types of data brought the final number of NOAA/NESS test cases to 5. In addition, 4 test cases using NEPRF SPADS winds in place of NOAA/NESS winds, unrestricted by SMMR characteristics, were chosen. For reference, the 9 test cases are listed in Table 3. The NOAA/NESS analysis times are chosen to correspond to available SMMR coverage. For the Pacific test case analysis times, SMMR data are available from 2100Z to 2400Z on the listed calendar dates. GBF (global band fields) and SST data in this case are acquired for 0000Z for the date following the listed calendar date, which is the same time. NOAA/NESS winds are acquired for times equal to the analysis time ± 3 hours. For example, for an analysis time of Feb 2, 1981 at 2400Z, NOAA/NESS winds are acquired from 2100Z on Feb 2, to 0300Z on Feb 3.

For the Atlantic cases, GBF and SST data are taken at 1200Z, and NOAA/NESS winds from 0900-1500Z. GOES images are always available within 15 minutes of the analysis time, for these Atlantic and Pacific cases.

Data for the four SPADS test cases were acquired in real time by NEPRF on Nov 22, 1982.

Table 3. Test cases

Test Case	Test Case No.	Calendar Date (1981)	Day of Year	Analysis Time (Z)	Lat/Lon Window Deg.	Ocean
NOAA/ NESS	1	Feb 2	33	2400	30S-20N/130-175W	Pacific
	2	Jul 24	205	2400	30S-40N/130-180W	Pacific
	3	Sep 8	251	1200	10-40N/40-60W	Atlantic
	4	Sep 14	257	1200	10-40N/40-60W	Atlantic
	5	Sep 30	273	1200	22-36N/35-75W	Atlantic
SPADS	6	Nov 22	326	1800	5-45N/50-80W	Atlantic
	7	Nov 22	326	1800	35-15S/73-88W	Pacific
	8	Nov 22	326	2200	10-50N/125-155W	Pacific
	9	Nov 22	326	2200	50-10S/125-155W	Pacific

SECTION 5

SOFTWARE

The algorithms developed for this task were implemented using the IBM-370/158-based hardware and software system in JPL's Image Processing Laboratory. The software executive is VICAR (Video Information Communication and Retrieval). The organization of the software is outlined in Figure 9. The various types of data arrive on magnetic tape and are first converted to a VICAR-compatible format. They are then interpolated to a common grid using the Endlich-Mancuso objective analysis routine, as described in Section 3. They are integrated into one comprehensive file in a merging routine, in which the wind veering algorithm described in Section 2 is implemented. The GOES images are map-projected from their original perspective into a simple rectangular projection, i.e., lines of latitude and longitude are straight, perpendicular, and equally spaced. Various display and summary routines are used to analyze the results, e.g., overlaying the wind vectors on the map-projected GOES image.

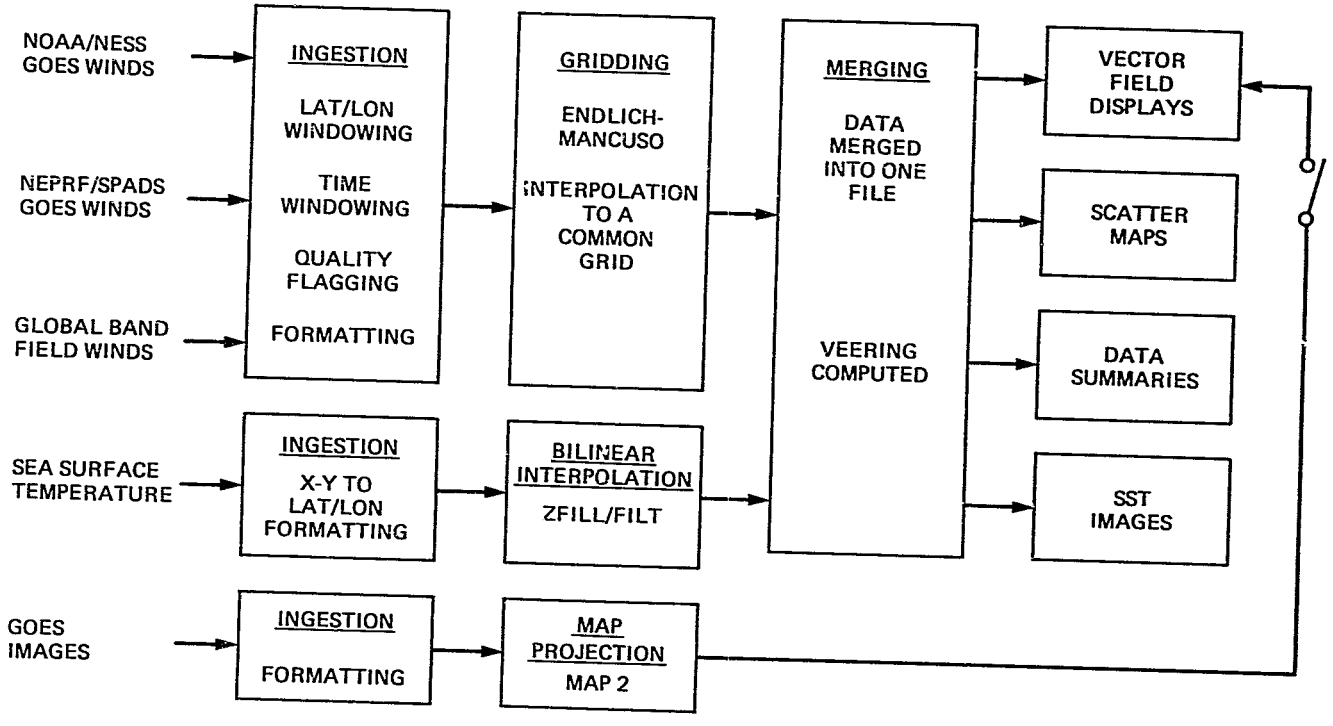

Figure 9. Software architecture

SECTION 6

TEST-CASE PROCESSING

For the nine test cases listed in Table 3 (Section 4.3), the main and ancillary data were acquired on magnetic tape from the sources listed in Table 2 (Section 4.1). For test cases 1-5, the satellite winds were supplied by NOAA/NESS. For test cases 6-9, they were supplied by NEPRF, from the SPADS system. The remainder of the data types (Global Band Fields, Sea Surface Temperatures, and GOES images) were identical for all test cases.

The first step in test-case processing is to "ingest" all the data, i.e., read the data and convert them to VICAR-compatible format. The ingesters select observations within a latitude/longitude window and within an analysis time window. For SST and GBF data, it is possible to read files for times bounding the analysis time and interpolate, if desired. A wind speed cutoff can be employed. For SPADS winds, the quality factor supplied with the data is used to reject bad points. The cloud-tracked wind data are usually restricted to pressures greater than (altitudes less than) 850 mbars. The wind data are output from the ingesters as spot data in the form (lat, lon, U comp, V comp) or (lat, lon, speed, direction) plus associated parameters.

GOES images are acquired from the University of Wisconsin, where they are archived on video tape. This system often results in dropped lines and blocks, and occasional garbled images, but good images were ingested for all NOAA/NESS test cases (GOES images for the SPADS cases were supplied directly by NEPRF).

SST data are read separately from Northern and Southern hemisphere files, and polar stereographic grid positions are converted to latitude and longitude. Figures 10a and b illustrate the SST processing for the NEPRF SPADS test cases 6 and 8, respectively. Each leftmost image ("Raw") in Figure 10 shows the result of the conversion of SST positions from the 63x63 FNOC polar stereographic (i,j) grid to rectilinear (lat, lon). A dot is placed at the corresponding (line, sample) for each SST data point in the test case window. The brightness of the dot corresponds to the SST magnitude.

Each central image ("ZFILL") in Figure 10 shows the result of applying an algorithm that "grows" each data point outward in all directions with successive application of a 3x3 pixel window, until it encounters the region grown out from the neighboring pixel. Each grown region is of constant brightness, equal to the brightness of the data point. Each rightmost image ("FILT") shows the result of passing a convolutional low-pass filter over the grown image. This growing and filtering process is functionally equivalent to bilinear interpolation. The filter size was large enough to smooth the data, but small enough not to oversmooth the data, which would result in a measure of the SST gradient lower than the actual value.

The first image in Figure 11 shows the interpolated SST image for case 2. The second and third images show the result of computing the SST gradient magnitude and direction, respectively. The gradient magnitude is displayed as scaled pixel brightness. The gradient direction clockwise from north is similarly displayed. Although the contrast stretch of the latter image renders visual interpretation difficult, its numerical content is correct. The possible anomaly near the equator is of no consequence because the SST data within 10° of the equator are not used in the veering computation. A 2.5°x2.5° mesh of points is used to pick off the corresponding SST gradient information from the magnitude and direction images.

After the GBF, NOAA/NESS, and SPADS data are ingested, they are gridded with a 2.5° mesh using the Endlich-Mancuso technique. This produces a grid whose boundary is one mesh distance in from the boundary of the ingested test area. Where necessary, the data are converted from (speed, direction) to (U,V) before gridding.

The GOES images are map-projected from the perspective projection of the GOES satellites to a rectangular (simple cylindrical) projection, in which lines of latitude are horizontal, straight, and equally spaced, and lines of longitude are vertical, straight, and have the same equal spacing. The left and right sides of the GOES image are thus curved. The map-projection program MAP2 requires the following input: sub-spacecraft lat/lon, image center lat/lon, north angle, and the scale in pixels per km at the focal plane. The image center and scale were initialized and refined using measurements made from a full-disc NOAA GOES image for the same time, containing a lat/lon grid superimposed by NOAA.

All data are then merged into a common file. NOAA/NESS and SPADS data are veered, using the technique described in Section 2. Vector fields with and without GOES images in the background, scatter maps, and data summaries are then produced.

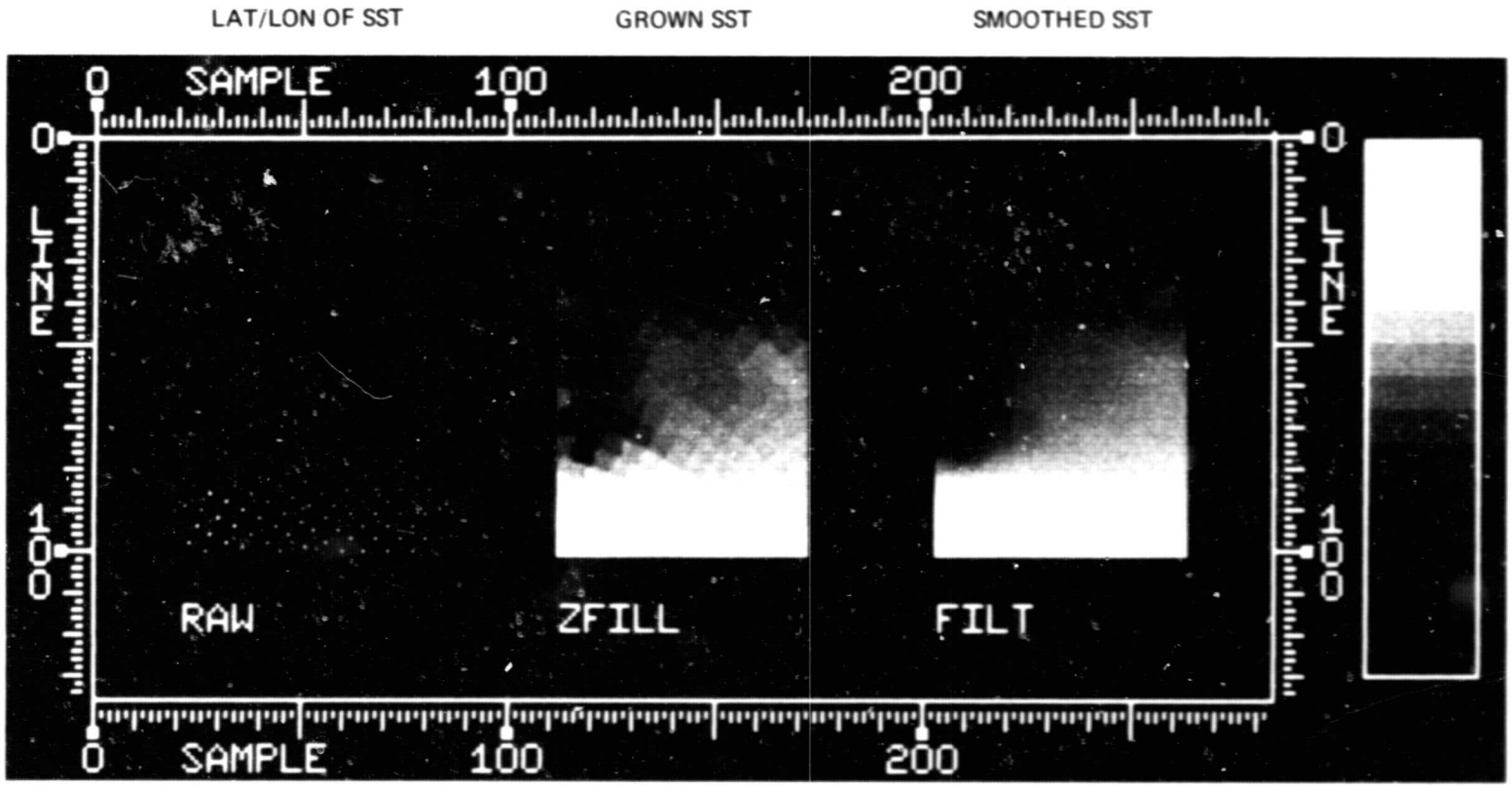

Figure 10a. SST data for case 6

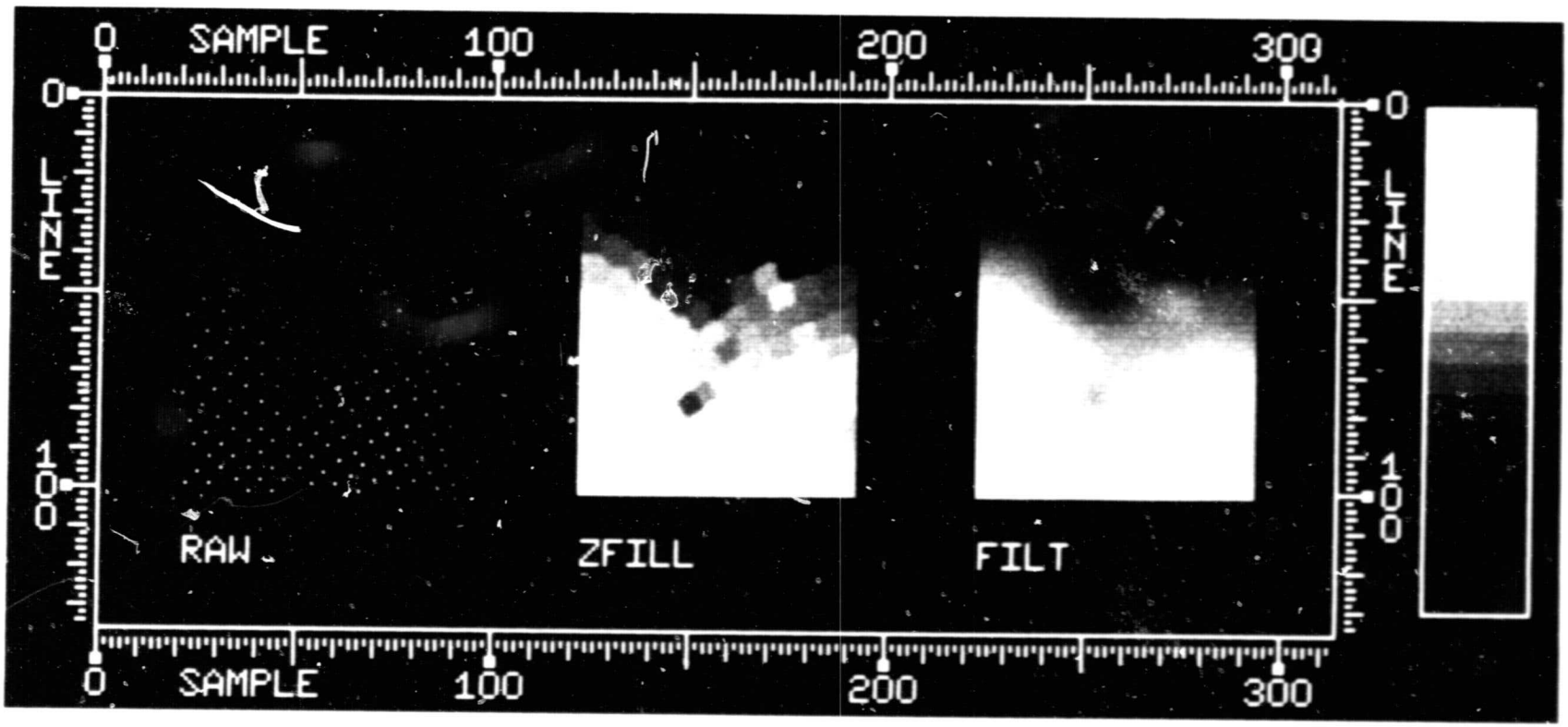

Figure 10b. SST data for case 8

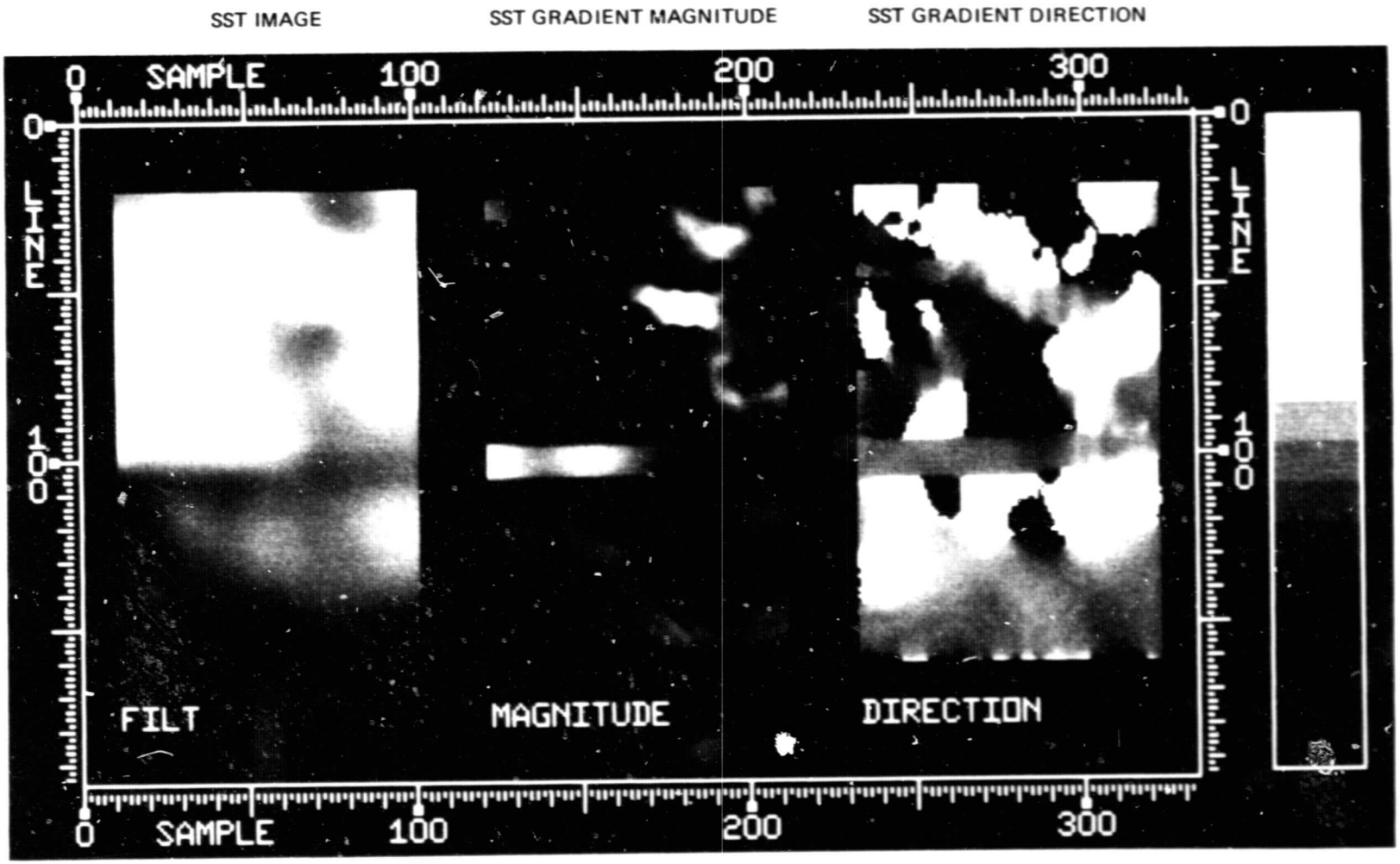

Figure 11. SST gradient data for case 2

SECTION 7

METEOROLOGICAL ANALYSIS

For each of the nine test cases, the effect of the veering algorithm was examined by first constructing a best-guess wind direction field based on the surface wind global band field, GOES visual and infrared imagery, and meteorological intuition. The unveered and veered cloud wind fields were then compared subjectively to the guess field to determine whether the overall effect of the veering was positive, negative, or neutral. Occasionally, the cloud wind fields lacked raw data in some areas, or were tracking clouds at too high a level, and this had to be taken into consideration. Vorticity and divergence fields were also constructed from the wind fields, and the magnitudes and positions of major features were compared. Generally these fields did not add any significant new information that could not be discerned from the wind vector fields, and so for the sake of brevity are not shown.

In the following, a meteorological description is given for each case, along with a comparison of the global band field, and unveered and veered cloud wind fields. Each case is accompanied by figures of the raw GOES images, by map-projected GOES images with veered cloud wind vectors, and by plots of the best-guess wind directions, the global band field, the gridded cloud wind vectors, and the veered cloud wind vectors. (Note that the plots show all of the vectors, while the GOES figures are missing part of the northernmost vectors. This results in missing partial or full lines. Latitudes are marked on all figures.)

Case: Feb 2, 1981, 2400 Z (Figures 12-14)
27.5 S - 17.5 N Lat, 132.5-172.5 W Lon

This case covers a large area in the tropical Pacific. The ITCZ is well-established from 0N, 170W to 8N, 132W. There is another convergence line extending from 12.5S, 172W to 16S, 132W, with a compensating divergence zone centered near the equator at about 3S. There is an isolated tropical storm at 22S, 178W, and a large extratropical low at 50S, 170W. Four large cumulus clusters are found at 11S, 167W, at 21S, 167W, at 27S, 159W, and at 32S, 153W.

The global band field does not perform well in this case. The ITCZ and the convergence zone are defined poorly, and the trade winds south of the equator are generally rather light. The flow into the clusters and into the low at 22S is suggested well.

The gridded NESS wind field is also vague in the vicinity of the ITCZ and the equatorial divergence zone. The flow is much too southerly north of the ITCZ. The flow into the low at 22S is much better resolved, however.

The veered NESS wind field improves significantly on the unveered field in most areas. The ITCZ is much better defined, the winds north of the ITCZ

become more easterly, and the trades south of the ITCZ become more northerly, increasing the convergence in this area. The convergence area south of the equatorial divergence zone remains unresolved. There is some degradation of the local northerly flow into the cumulus clusters in the SW corner of the study area. The greatest improvement is seen in the trade winds converging on the ITCZ.

Case: Jul 24, 1981, 2400 Z (Figures 15-17)
27.5 S Lat - 37.5 N Lat, 132.5-177.5 W Lon

This case covers a wide variety of tropical and extratropical meteorological features. A distinct shear zone extends from 35N, 150W to 51N, 128W, separating a storm system to the northwest from a stratus-laden circulation to the southeast. The remnants of a low at 25N, 136W and a vorticity maximum at 22N, 142W lie southwest of the high, with a convergence line extending from 20N, 120W to 29N, 135W, and a col point at 30N, 155W. Another convergence line extends from 15N to 30N at 180W. The ITCZ has a prominent wave crest at 12N, 160W, but is rather broken east of 150W. The flow south of the ITCZ consists mostly of SE trades, with a convergence line running SE from 8S, 180W.

The global band field behaves surprisingly poorly in the Northern hemisphere. It tends to neglect the strong convergent flow into the low at 48N, 170W, as well as the ITCZ and the decaying storm system at 20-25N. In the Southern hemisphere, the trade winds and convergence zone are generally reproduced well, with the exception of the false convergence at 5S, 147.5W.

The gridded NESS wind field improves significantly on the flow into the low at 48N, and clearly suggests the wave on the ITCZ, but misses the convergence area in the SW corner of the study area. The NESS field also fails to identify the system at 20-25N.

The veered NESS wind field generally improves on the unveered field. The flow into the low at 48N and in the vicinity of the wave on the ITCZ at 160W exhibits better shape. The trade winds south of the ITCZ are generally more northerly than for the unveered field. This results in a slight improvement in the SW region, and a slight deterioration in the SE region. The veering does not enhance the convergence in the SW corner.

Case: Sep 8, 1981, 1200 Z (Figures 18-20)
12.5-37.5 N Lat, 42.5-57.5 W Lon

The meteorology within the study area is not exceptional, but it is surrounded by several tropical storms, located at 15N, 65W, at 42N, 52W, and at 32N, 65W, in addition to a developing wave on the ITCZ at 10N, 50W, and a small wave in the trades at 25N, 39W. A ridge of high pressure is vaguely defined at about 25N latitude.

In general, the global band field is in good agreement with these features, with the possible exception that it flattens out the wave in the ITCZ at

10N latitude and places the high at a lower latitude than is suggested by the satellite photos.

The gridded NESS wind field is in reasonable agreement with the global band field except in the regions of the two tropical storms to the west of the study area. In the case of the tropical storm at 15N, the NESS field shows the trade winds blowing rather straight into the low. Since the storm is rather compact, it is difficult to say which analysis is better in this region. In the case of the tropical storm at 32N, the gridded NESS wind field clearly suffers from a lack of raw wind vectors in the region and gives less indication of a cyclonic flow nearby. The NESS gridded field does give some indication of the convergence and wave structure at 35N, 45W, which is completely smoothed over by the GBF.

The veered NESS wind field improves on the unveered field in some areas, and does no harm to the analysis anywhere. Naturally, the tropical storm at 32N remains unresolved, but the winds flow more readily into the tropical storm at 42N. The pattern in the SW corner displays more divergence into the cloudless area, with some winds possibly tracking around the cyclonic feature at 10N, 50W.

Case: Sep 14, 1981, 1200 Z (Figures 21-23)
12.5-37.5 N Lat, 42.5-57.5 W Lon

There is comparatively little action within the study field, although once again there are prominent features just outside: a tropical storm at 40N, 40W, and a hurricane at 26N, 62W. The enlarged satellite photo shows considerable flow at all levels into the hurricane from the southeast, enhanced by the large high centered at about 28N, 50W. Just north of the convergence into the hurricane is a sharp convergence zone, which may extend out from the tropical storm at 40N. A weak front extends out of a low at 52N, 50W, down to the north edge of the study area at 36N, 55W.

The global band field captures the salient features on the GOES imagery rather well, with the usual exception that the convergence line has basically been smeared out. There is a single unexplained vector in the NE corner of the study area.

In a replay of the Sep 8 case, the gridded NESS wind field is quite consistent with the global band field, with the notable exception being in the vicinity of the hurricane. Once again, there is a lack of NESS raw winds in this region, and so the strong cyclonic flow goes unresolved.

The veering algorithm tends to have a somewhat negative impact for this case. In general, the unveered NESS field has no sharp gradients, and so the impact of the veering is not pronounced. The veered NESS field improves slightly on resolving the ITCZ feature at 10N, 50W, but tends to flatten out the flow in the north of the study area so that the tropical storm is no longer indicated.

Case: Sep 30, 1981, 1200 Z (Figures 24-26)
23.5-33.5 N Lat, 37.5-72.5 W Lon

The only dominant features for this case are the hurricane at 40N, 42W, and the high centered at about 33N, 75W. A convergence line extending from 26N, 44W to 33N, 36W may or may not be connected with the hurricane. A weak front extends out of a low at 50N, 63W down to 30N, 60W. Its effect is not apparent in the field.

Although there are relatively few features to reproduce, the global band field extends the anticyclonic flow too far east beyond 65W. Both the hurricane and the convergence zone seem to be well matched between the satellite imagery and the GBF.

Although there are no raw NESS wind vectors in the divergence area around 27N, 60W, the gridded NESS wind field resolves the flow around the high rather well, placing its center southward of the GBF analysis. There is no reason to believe that either analysis is better regarding the placement of the high. In the region of the hurricane and convergence zone, however, the NESS field is too flat and smooth. The gridding program also seems to have washed out some feature indicated in the SE corner of the raw NESS wind field.

Once again, due to the relative lack of features in the NESS field, the impact of the veering algorithm is negligible. The veered NESS field enhances the flow into the hurricane, but reduces the northerly component of the flow at 50W.

Case A: Nov 22, 1982, 1800-2000 Z (Figures 27-29)
7.5-42.5 N Lat, 52.5-77.5 W Lon

With winter approaching, the dynamics of the temperate zone become more prominent in this northern latitude case. The field is large enough to examine the morphology of the dominant double low at 30N, 66W, and at 35N, 65W, with a weak trough extending southward to 20N. A high is indicated at about 41N, 45W. A dynamically weak front in the NW corner of the study area extends from 34N, 85W to 45N, 67W, crossing a ridge which joins the high at 41N to another high over Quebec. The front eventually strengthens and links into a low at about 55N, 50W. The flow just north off the coast of South America is difficult to determine from the GOES imagery only.

The global band field duplicates the outer flow into the low at the surface fairly well, but misses the north partner of the double low. The whole pattern has also shifted rapidly in time, so that the major temperate zone features are all displaced meridionally from the satellite photographs. The GBF also puts the ridge somewhat farther north than the satellite photos.

The SPADS gridded wind field displays a significantly greater departure from the global band field than was the case with the NESS gridded wind fields. The SPADS wind field suggests the double low much better than the

GBF, but the outer flow into the low is not as realistic for surface flow as is the GBF analysis. Especially, the SPADS field on the northeast side of the double low is too northerly and divergent into the high at 45W. The cloud winds in the NW corner of the study field are probably correctly tracked by SPADS, but the surface analysis would seem to indicate that the surface winds are blowing in almost the opposite direction.

The SPADS veered field improves fairly significantly on the unveered field. In general, the flow into the double low now converges more strongly from all sides than in the unveered case. The flow in the northwest and southeast corners of the study area still differs markedly from the GBF, but shows better curvature into the rest of the field, with the largest improvement being the mitigation of some of the strong easterly component east of Haiti.

Case B: Nov 22, 1982, 1800-2000 Z (Figures 30-32)
32.5-17.5 S Lat, 75.5-85.5 W Lon

The meteorology in this case is rather limited, as is the size of the study area. Primarily, the flow is within a region of cumulus convection that is loosely connected to the high at 43S, 82W.

The global band field seems to misposition the high, causing the flow in the area to be too southerly, compared to the well-defined cloud bands in the satellite photographs.

The gridded SPADS wind field generally displays the winds correctly. For this case, the veering has a negative impact on the SPADS winds. The wind directions rotate clockwise to the surface, causing the flow to become too radially outward from the high.

Case C: Nov 22, 1982, 1800-2000 Z (Figures 33-35)
12.5-47.5 N Lat, 122.5-152.5 W Lon

Despite the relatively early date, this case displays several wintertime storms lined up to impinge on the west coast at relatively low latitudes. There is a fully developed low immediately off the coast at 40N, 129W, with a front extending down to 20N, 138W. A vorticity maximum exists at 35N, 134W. There are two more lows farther west: one at about 50N, 160W, with a front extending to 35N, 152W, and a large low at 45N, 175W. Also, there is an isolated tropical storm at 15N, 164W. A col point exists at 40N, 136W. The ITCZ is broken but defined at about 5N. The storms are rapidly moving, and the center of the high has remained south of the front.

The performance of the global band field is rather mixed. Above 30N the analysis is rather good, in view of the rapidly changing weather. The vorticity max at 35N is not analyzed. Below 30N and 130W, the flow should be more westerly and convergent on the front. The analyzed high at 28N, 137W is probably only an area of decreased westerly winds. In general, all the winds south of 28N and west of 140W should be more westerly until just

east of Hawaii, where they turn into the tropical storm. The clear areas centered at 12N, 150W, and 10N, 135W also suggest more westerly flow south of the front.

The SPADS gridded wind field departs rather drastically from the GBF in this case. Once again, the easterly flow to the north of the low at 40N is too weak, but the increased westerly flow everywhere behind the front down to 22N is probably more appropriate. With the exception of the vicinity of Hawaii, the field south of 22N and west of 137W agrees well with the features on the GOES-W photos. The flow east of 137W and south of the front seems to be picking up clouds near the subtropical jet.

The SPADS veered field does not seem to have the same beneficial impact in converging the winds on the low off the coast, as was the case for the double low in region A. Some additional convergence is noted along the front in the northwest corner of the study field. The quality of the field seems to be largely unaffected between 16N and 22N, where the westerly components are too high for the surface winds.

Case D: Nov 22, 1982, 1800-2000 Z (Figures 36-38)
47.5-12.5 S Lat, 122.5-152.5 W Lon

This case displays two prominent storm systems at high latitudes in the Pacific Antarctic region, with an anticyclonic region centered at about 35S, 142W. A front extends from 36S, 160W to 50S, 148W, then off the satellite photographs into one of the lows. The other low is at 51S, 118W, to which the convergence zone in the NE corner of the study area is ultimately connected.

In general, the global band field agrees rather well with all these features, except that the convergence is too weak in the NE corner, and the convergence in the SW corner is missing.

The gridded SPADS wind field is in general agreement with the synoptic scale features of the global band field, except that in the trade wind region, some higher-level clouds, which appear to be traveling in a direction nearly opposite to the surface winds, have been picked up. These wind vectors are all in the NE corner of the study area, particularly in the region of the convergence zone. The SPADS wind field also shows some convergence in the vicinity of the front in the SW corner.

For this case, the veering algorithm does not improve on the gridded SPADS wind field. The convergence in the vicinity of the front in the SW corner is enhanced, but the flow into the low at 50S becomes too direct. There is little difference in the trade wind region.

In summary, the effect of the veering was more beneficial than detrimental, and in no case was highly detrimental. The test cases spanned a variety of meteorological conditions including fronts, tropical and extratropical cyclones, anticyclones, trade winds, and the intertropical convergence zone. For the nine cases, the impact was judged to be positive for four

cases, negative for two cases, and neutral for three cases. The impact was most positive in regions of extratropical cyclones and the ITCZ, and most negative around large anticyclones. Generally, the dominant factor in the veering correction for the nine test cases was the dependence on latitude. The most significant departures from this behavior occurred in SPADS cases A and C in the vicinity of the extratropical lows, where perturbations of five to eight degrees with respect to the latitudinal contribution alone were observed. In both cases, the highest positive impact due to veering was observed in these areas. Future research should be directed toward increasing the coefficient of the advection term in equation (4), in order to determine if increasing the relative contribution of SST gradients has a beneficial effect on the results. As noted in Section 2.2, there is some prior indication that this should be investigated.

Table 4. JPL Photolab numbers for figures

Figure No.	JPL Photolab No.
10a	344-5058
10b	344-5060
11	344-5079
12	344-5091A
13	344-5042
15	344-5091B
16	344-5045
18	344-5092A
19	344-5033
21	344-5092B
22	344-5036
24	344-5093A
25	344-5039
27	344-5093B
28	344-5048
30	344-5094A
31	344-5051
33	344-5094B
34	344-5054
36	344-5095
37	344-5057

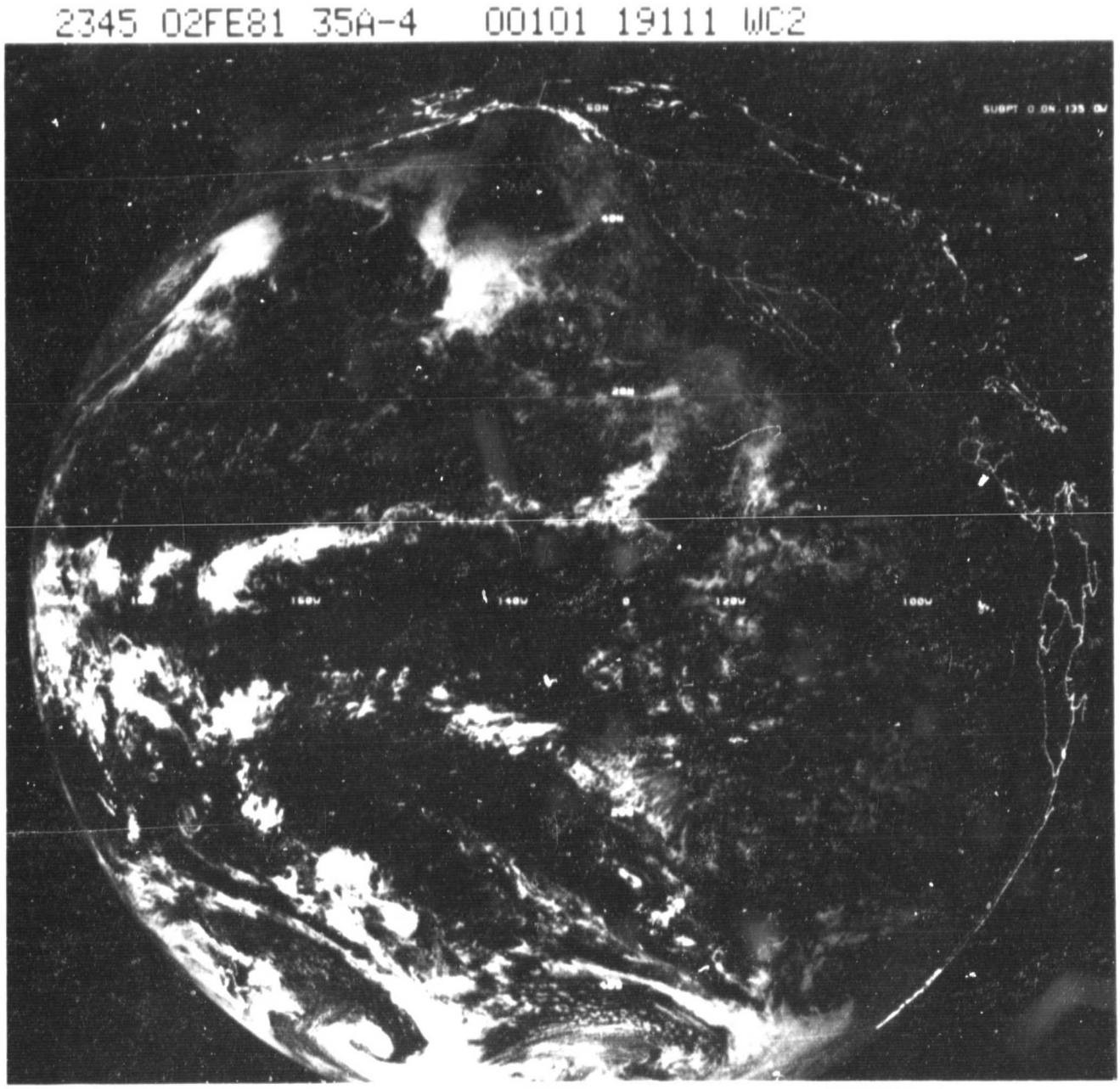

Figure 12. Raw GOES image for Feb 2, 1981 case

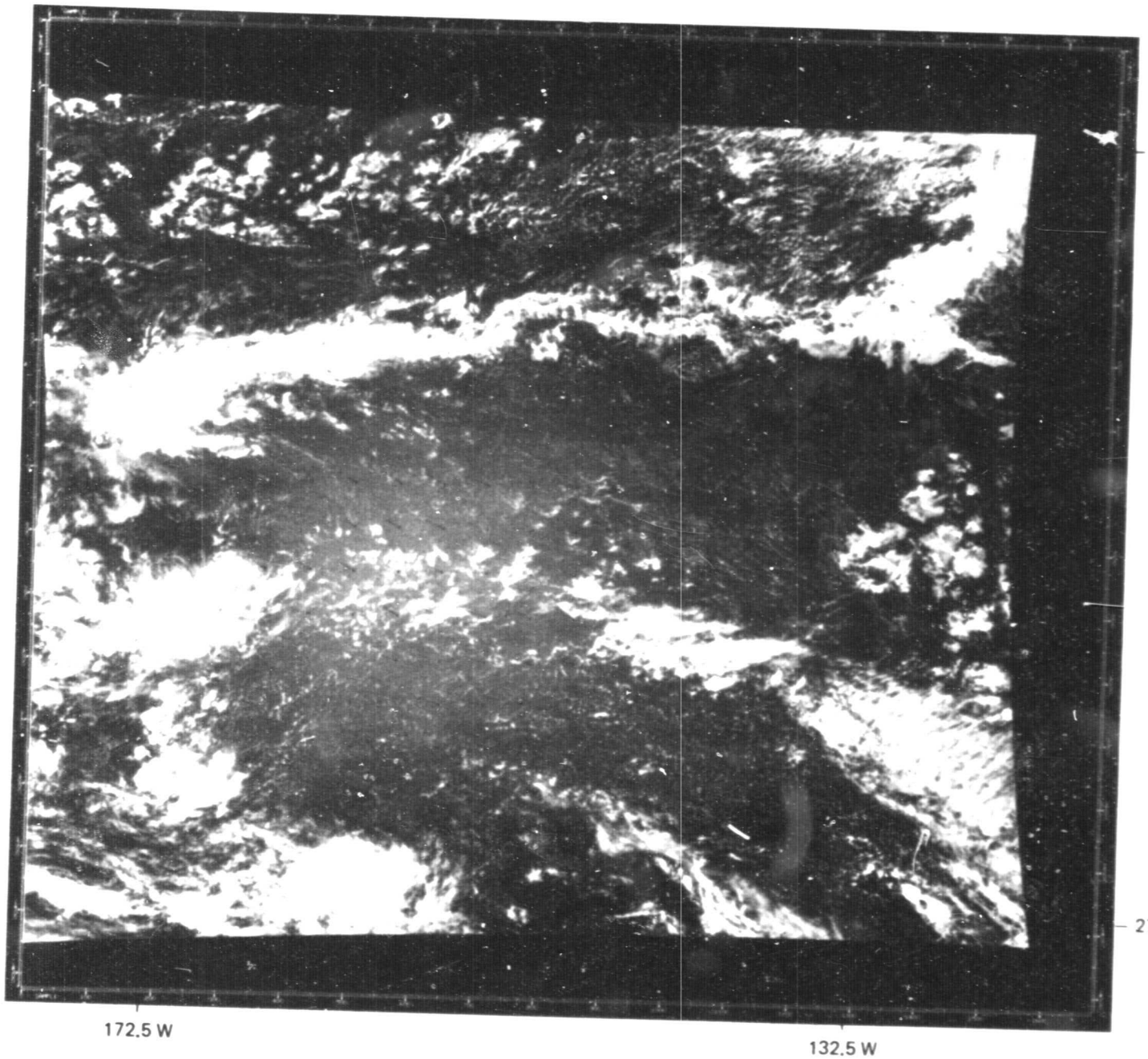

Figure 13. Veered NESS winds for Feb 2, 1981 case

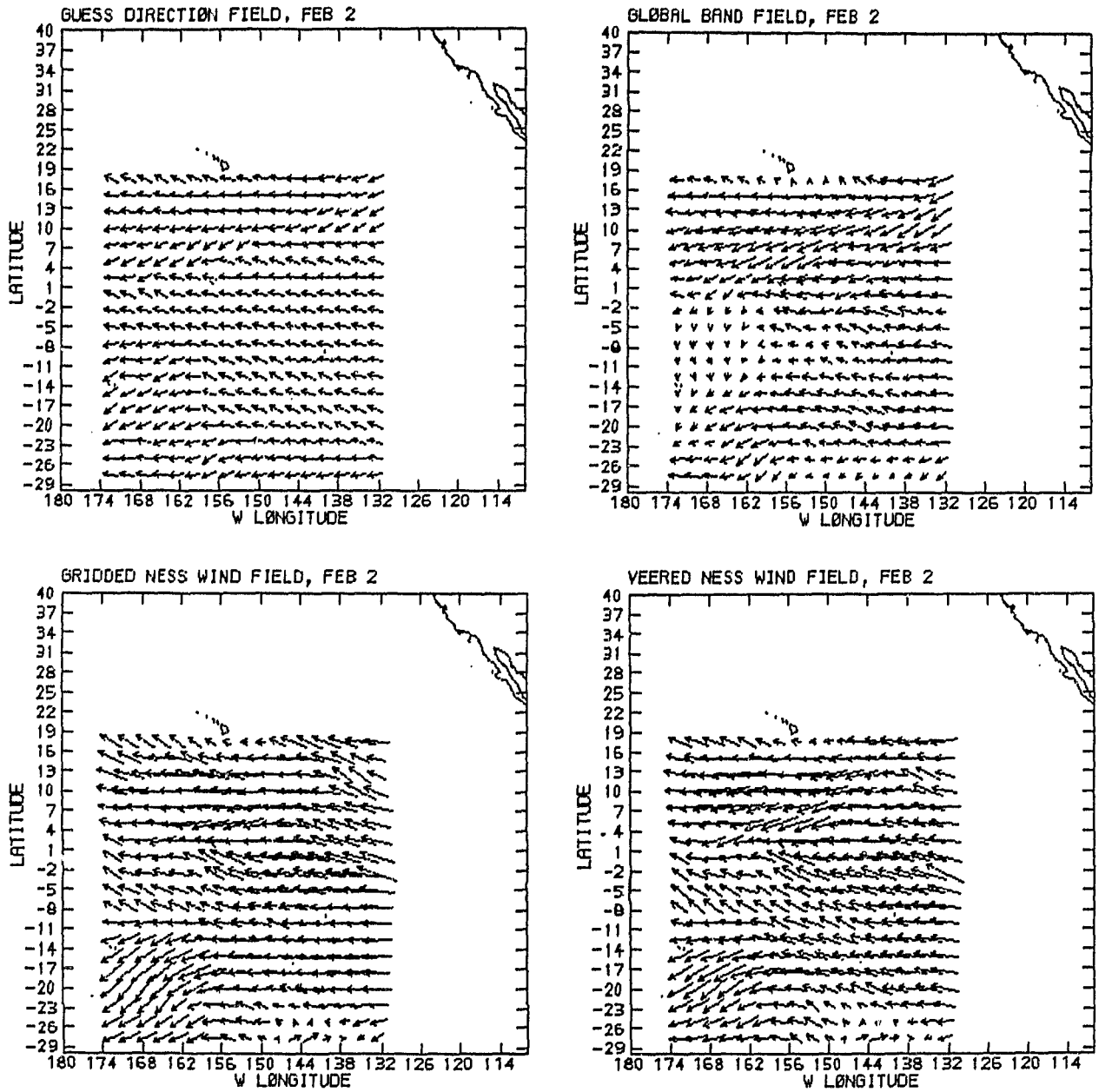

Figure 14. Wind vector plots for Feb 2, 1981 NESS case

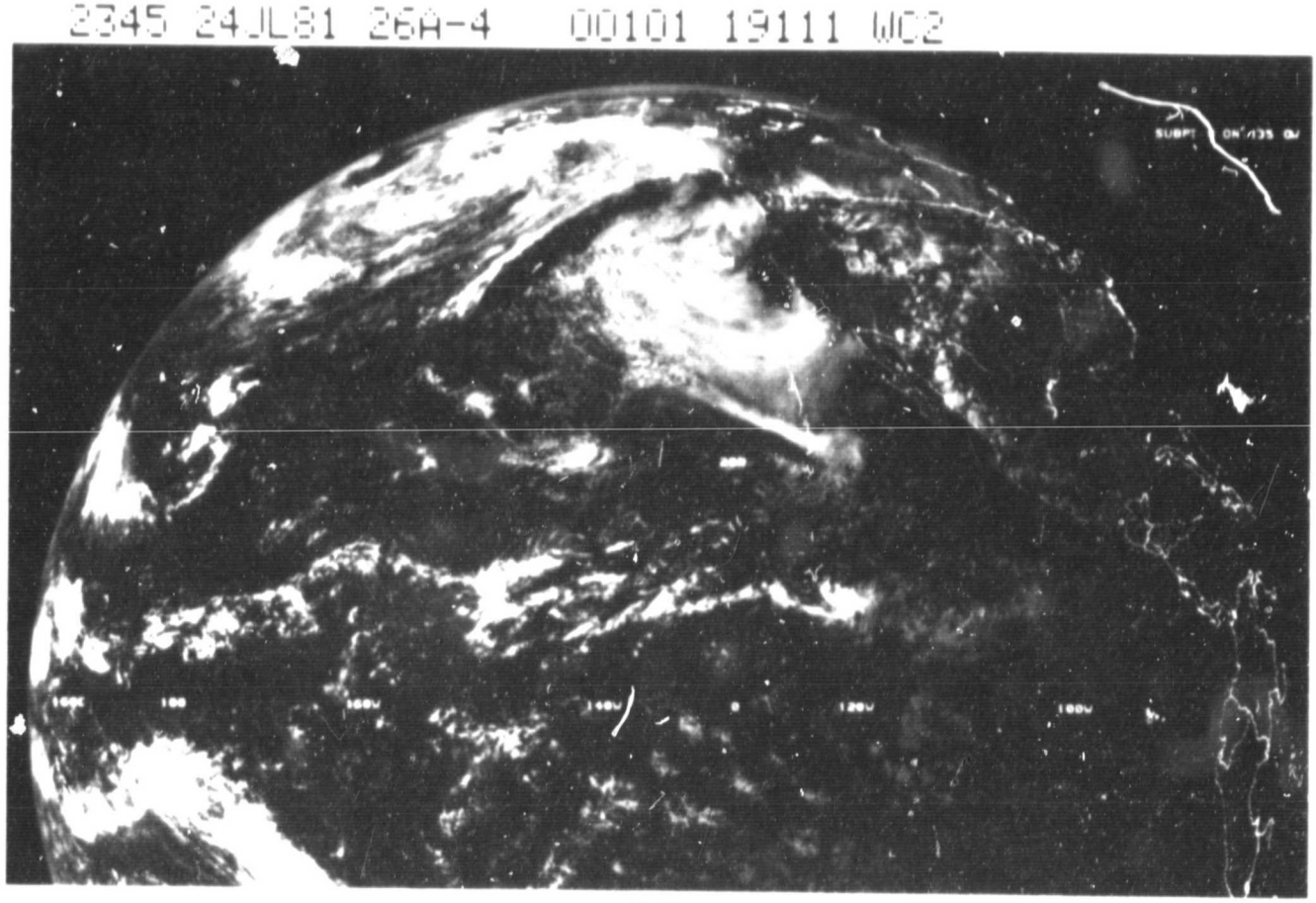

Figure 15. Raw GOES image for Jul 24, 1981 case

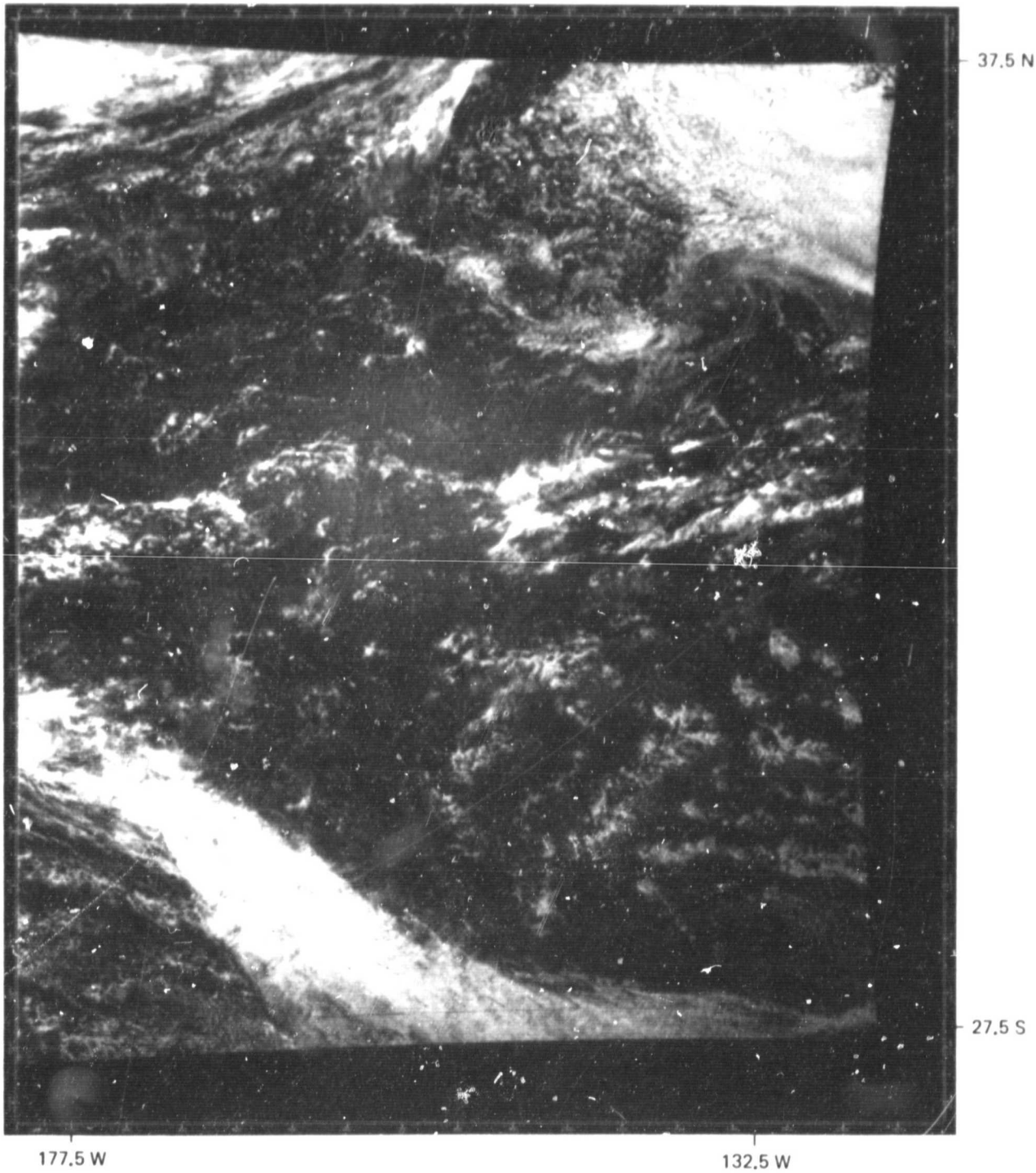

Figure 16. Veered NESS winds for Jul 24, 1981 case

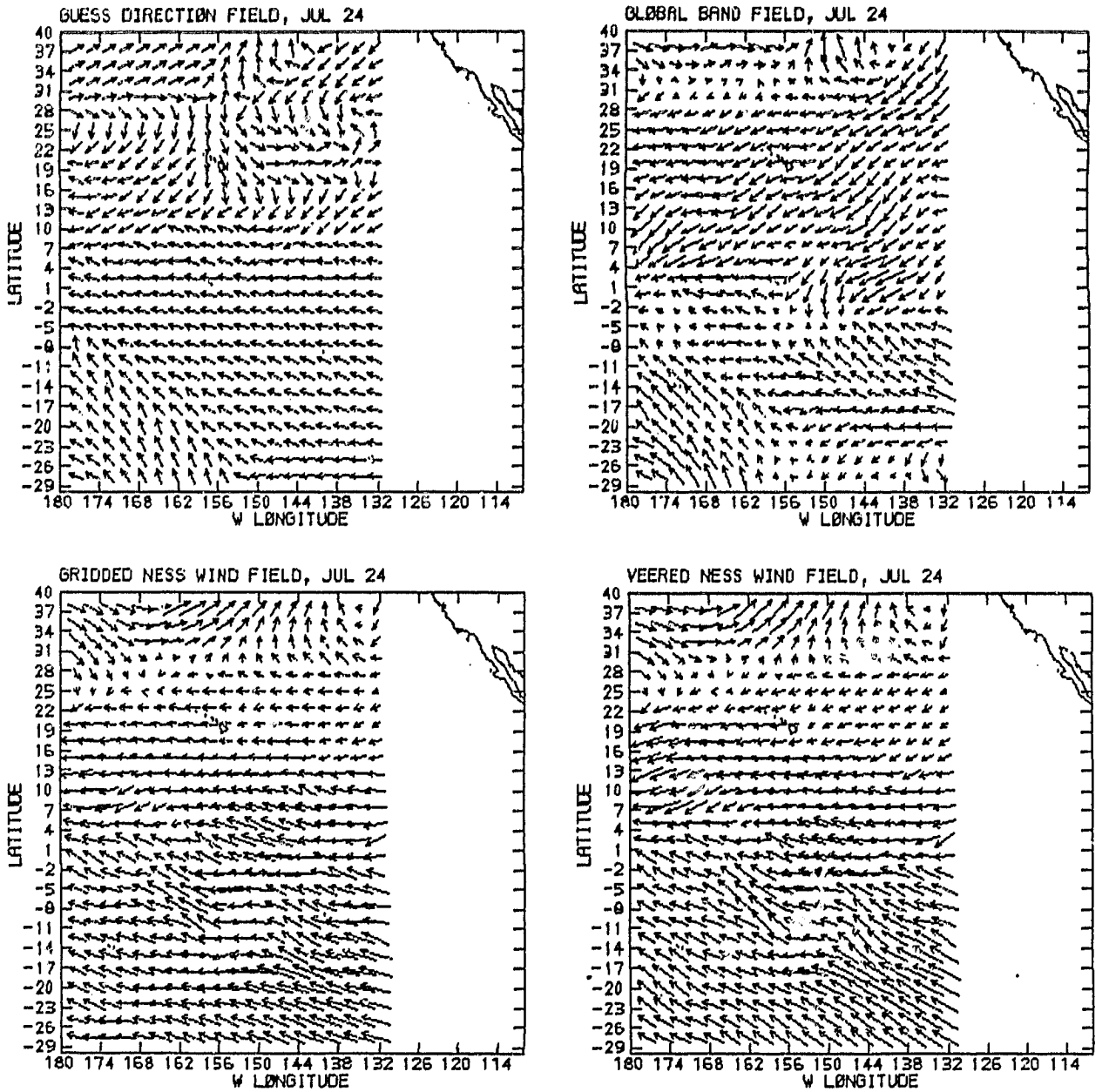

Figure 17. Wind vector plots for Jul 24, 1981 NESS case

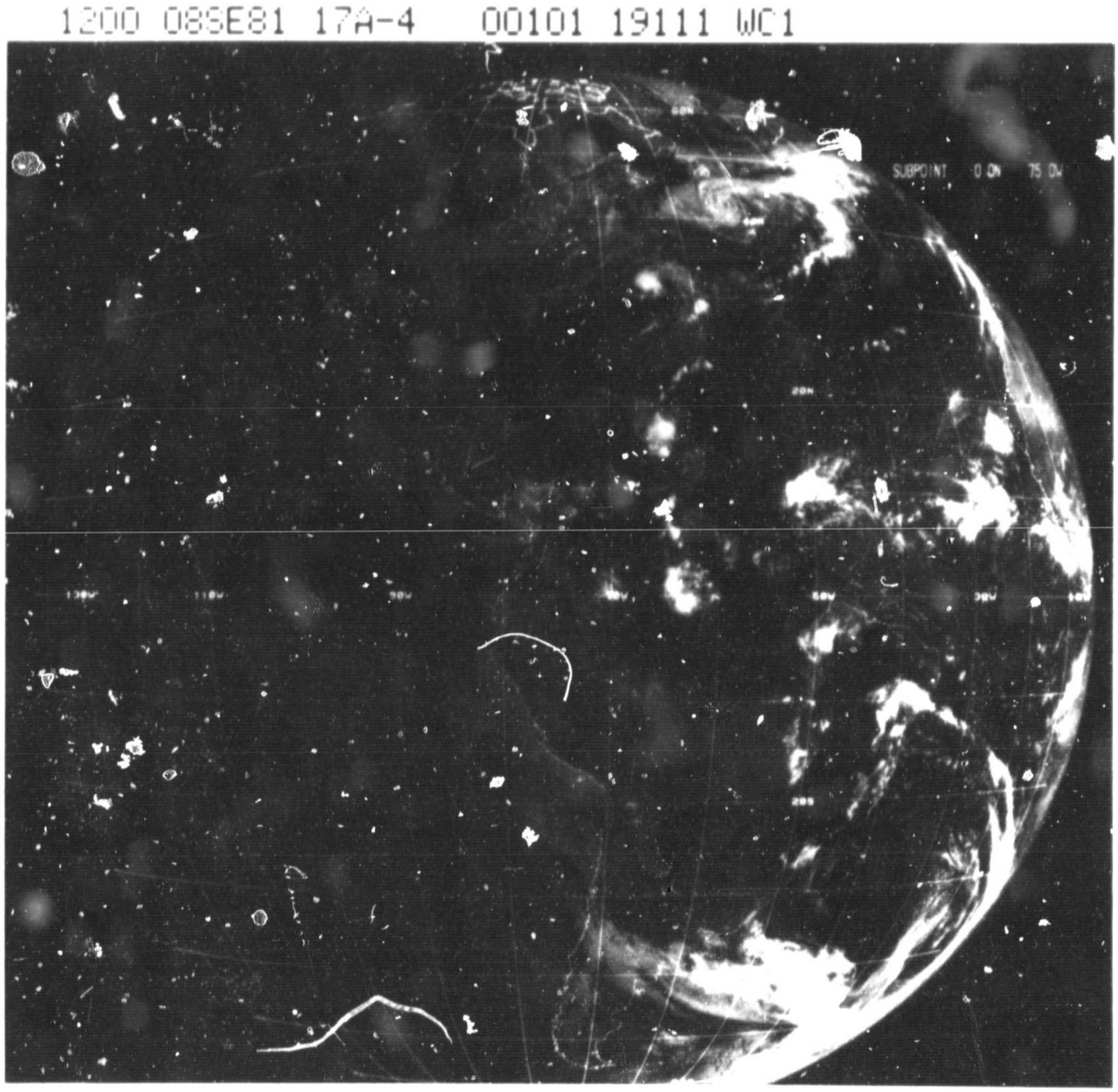

Figure 18. Raw GOES image for Sep 8, 1981 case

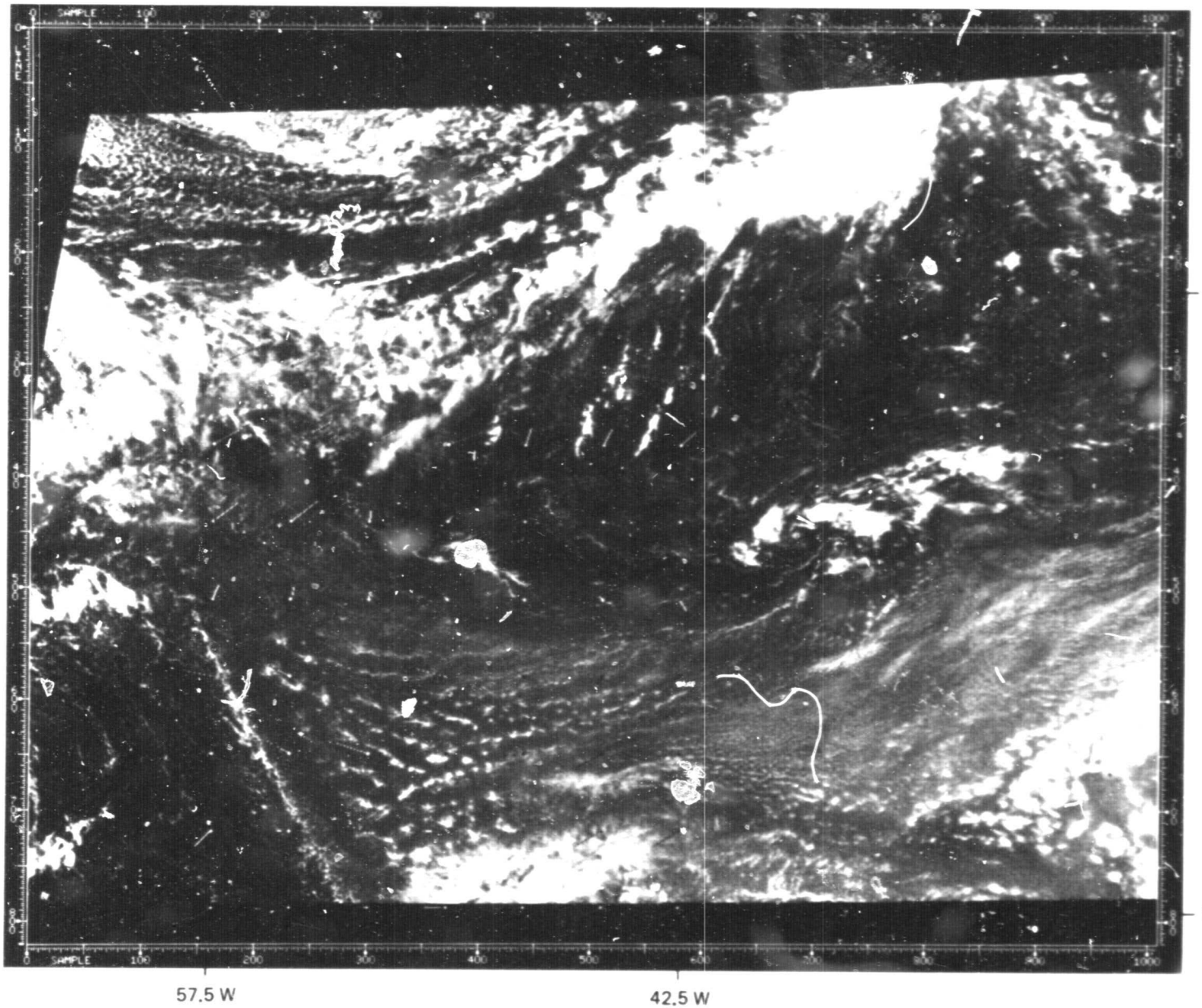

Figure 19. Veered NESS winds for Sep 8, 1981 case

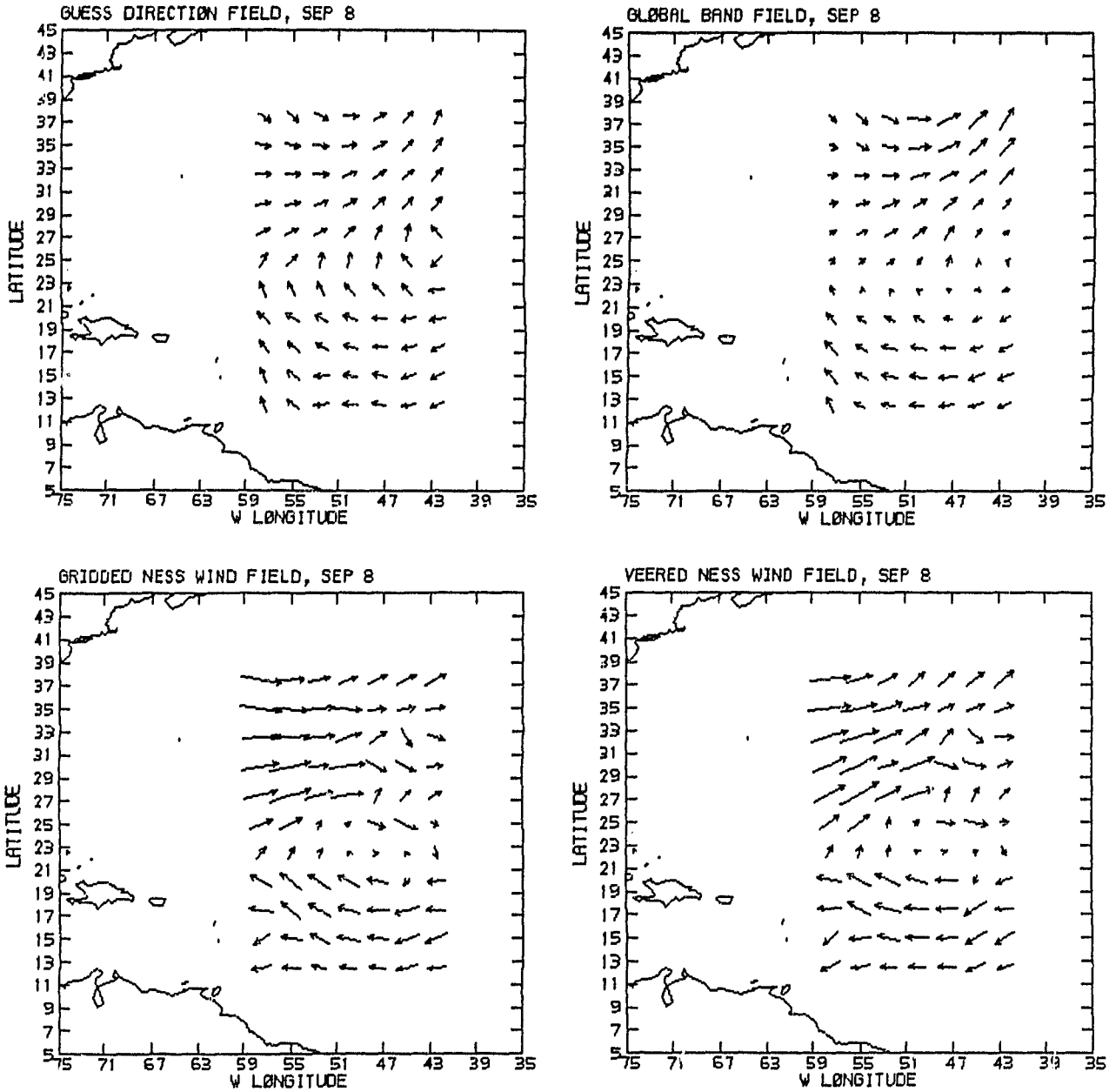

Figure 20. Wind vector plots for Sep 8, 1981 NESS case

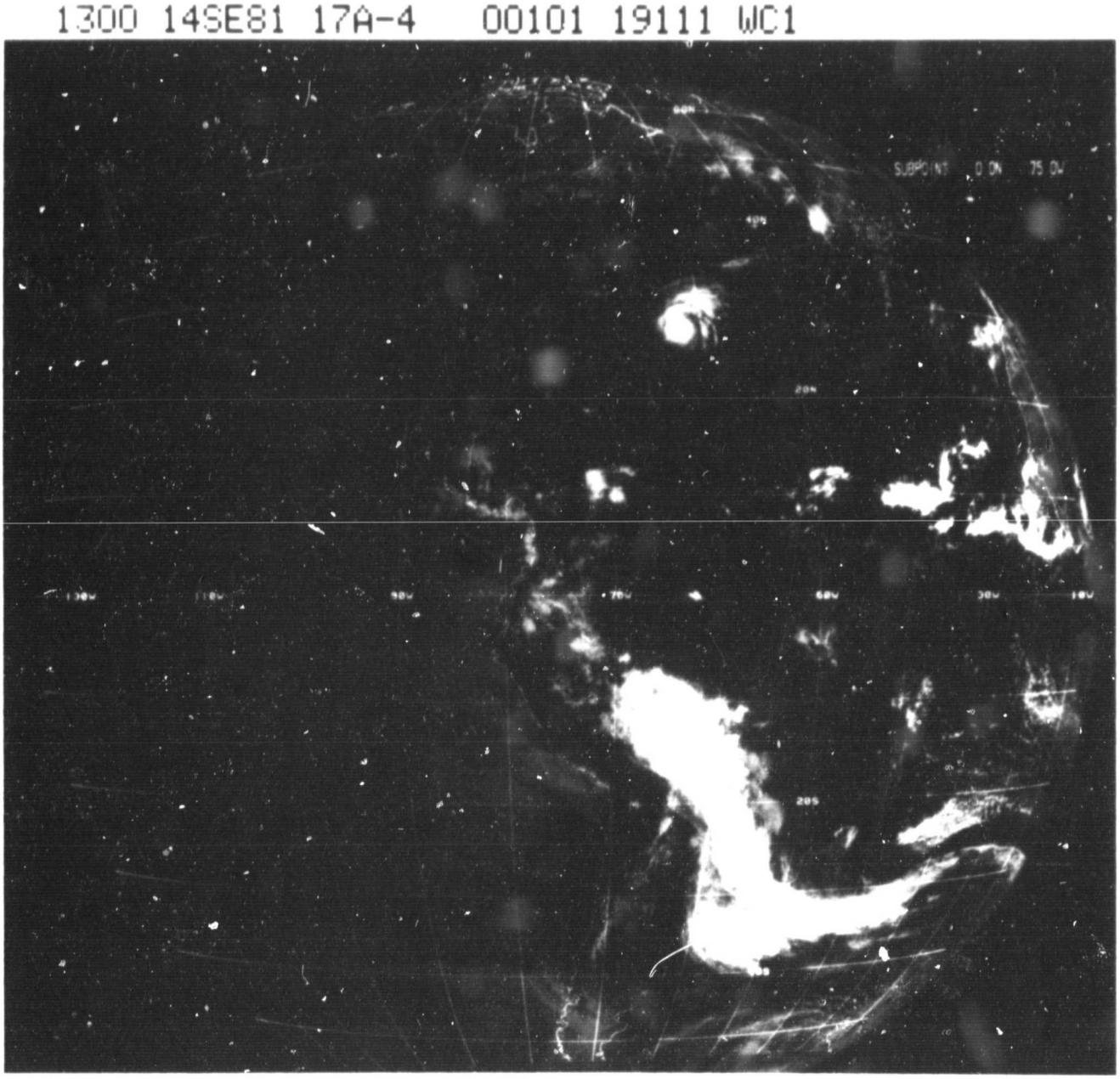

Figure 21. Raw GOES image for Sep 14, 1981 case

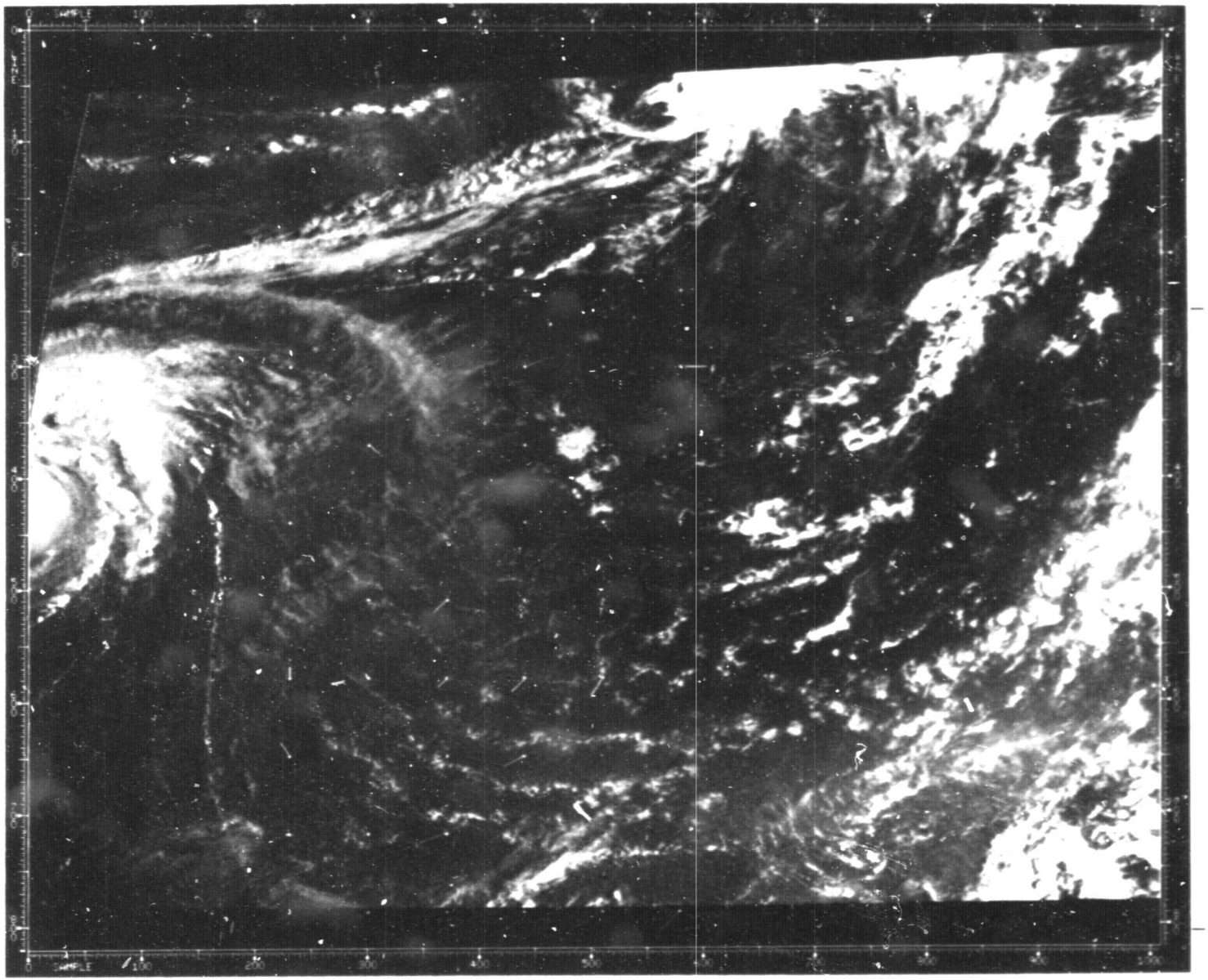

Figure 22. Veered NESS winds for Sep 14, 1981 case

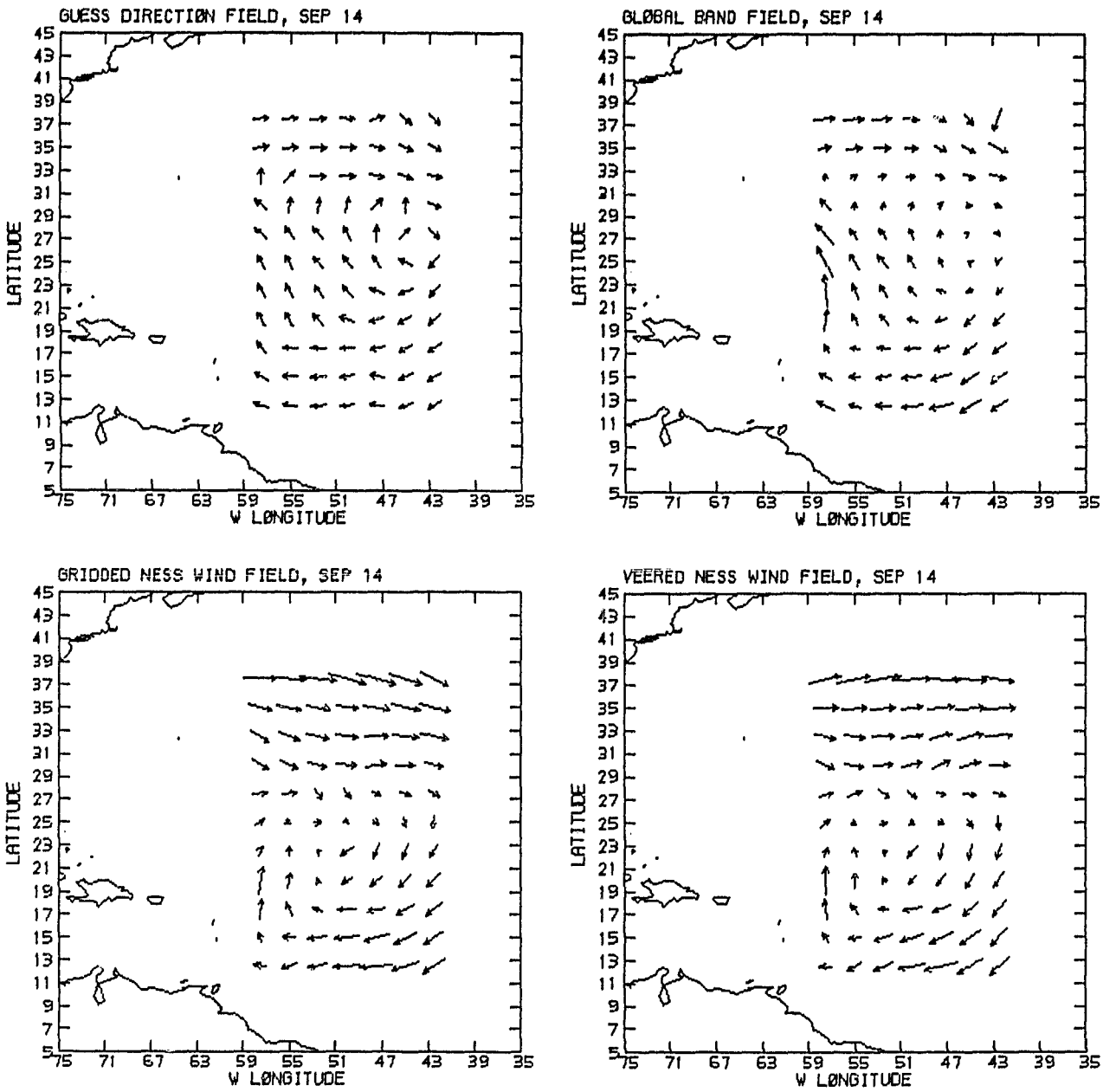

Figure 23. Wind vector plots for Sep 14, 1981 NESS case

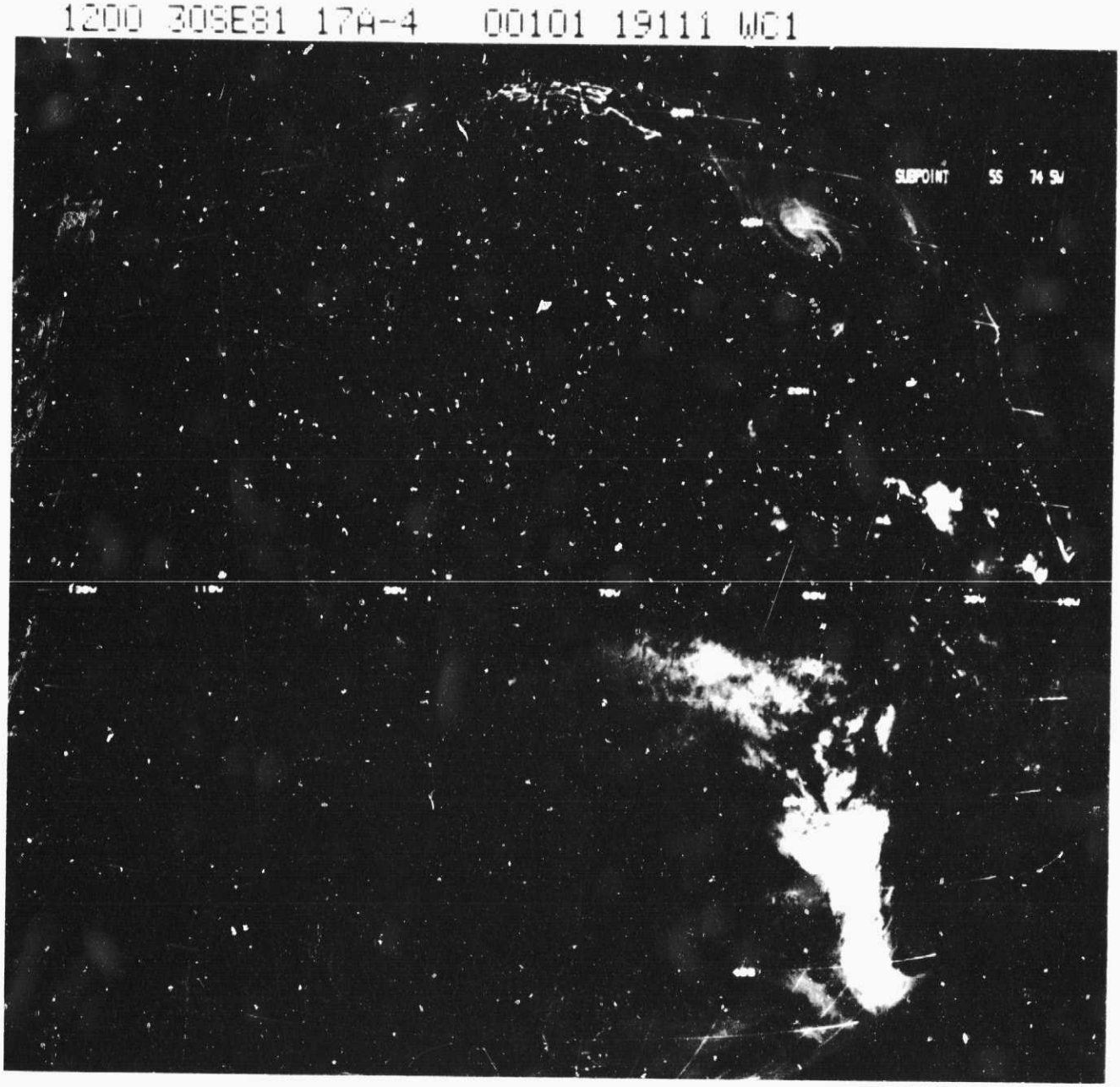

Figure 24. Raw GOES image for Sep 30, 1981 case

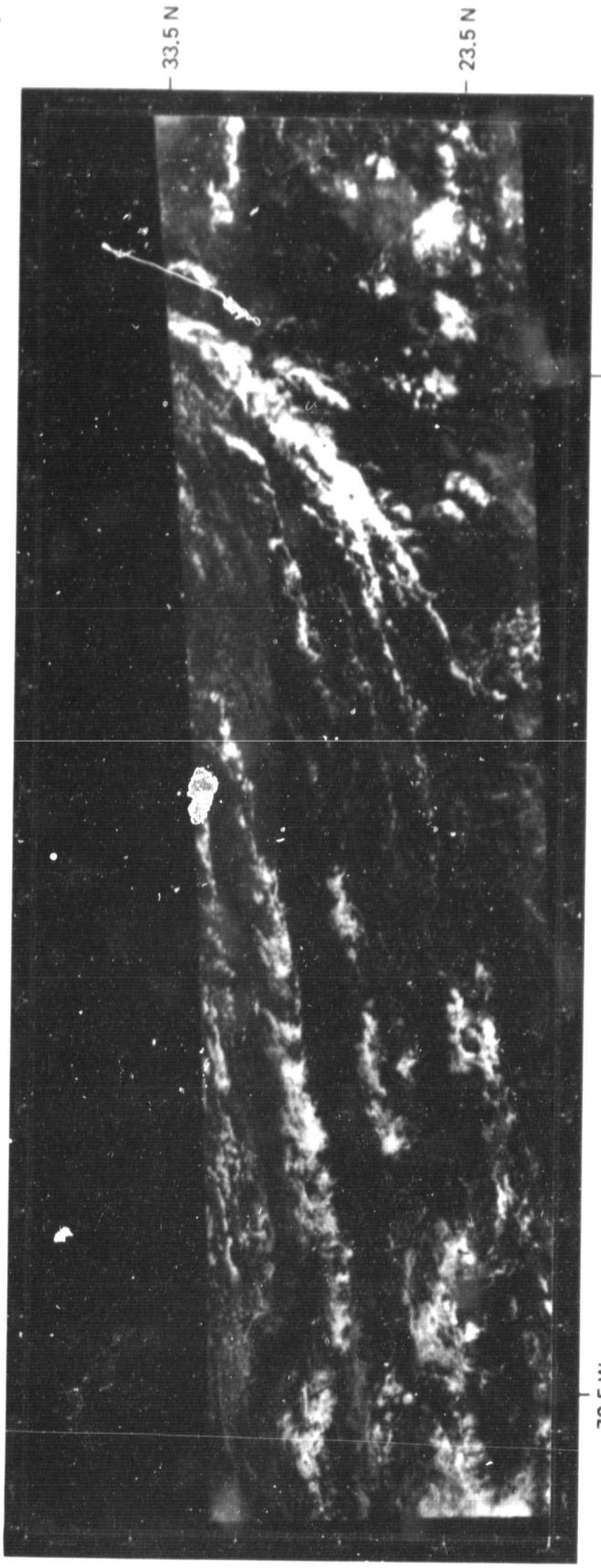

Figure 25. Veered NESS winds for Sep 30, 1981 case

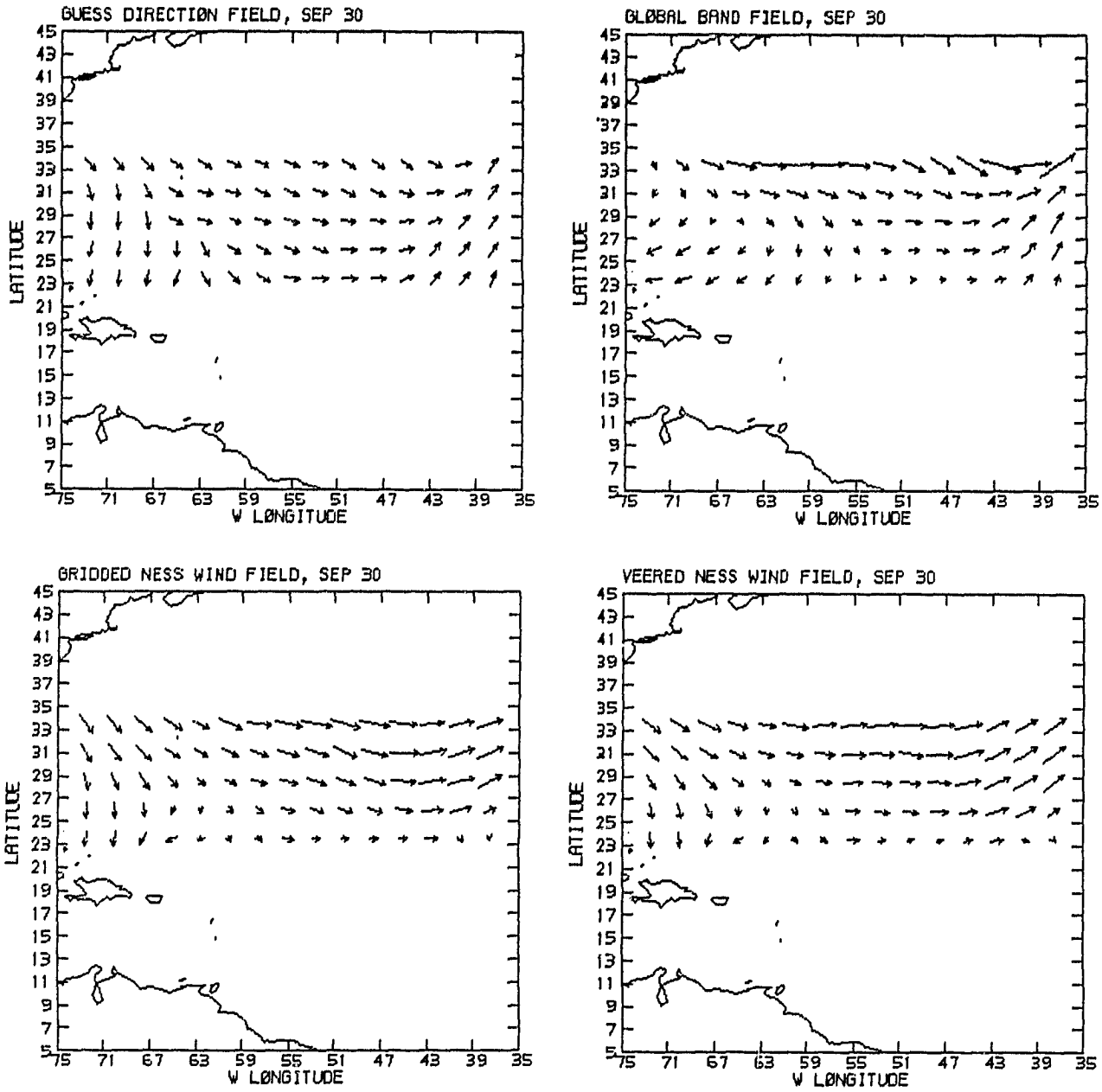

Figure 26. Wind vector plots for Sep 30, 1981 NESS case

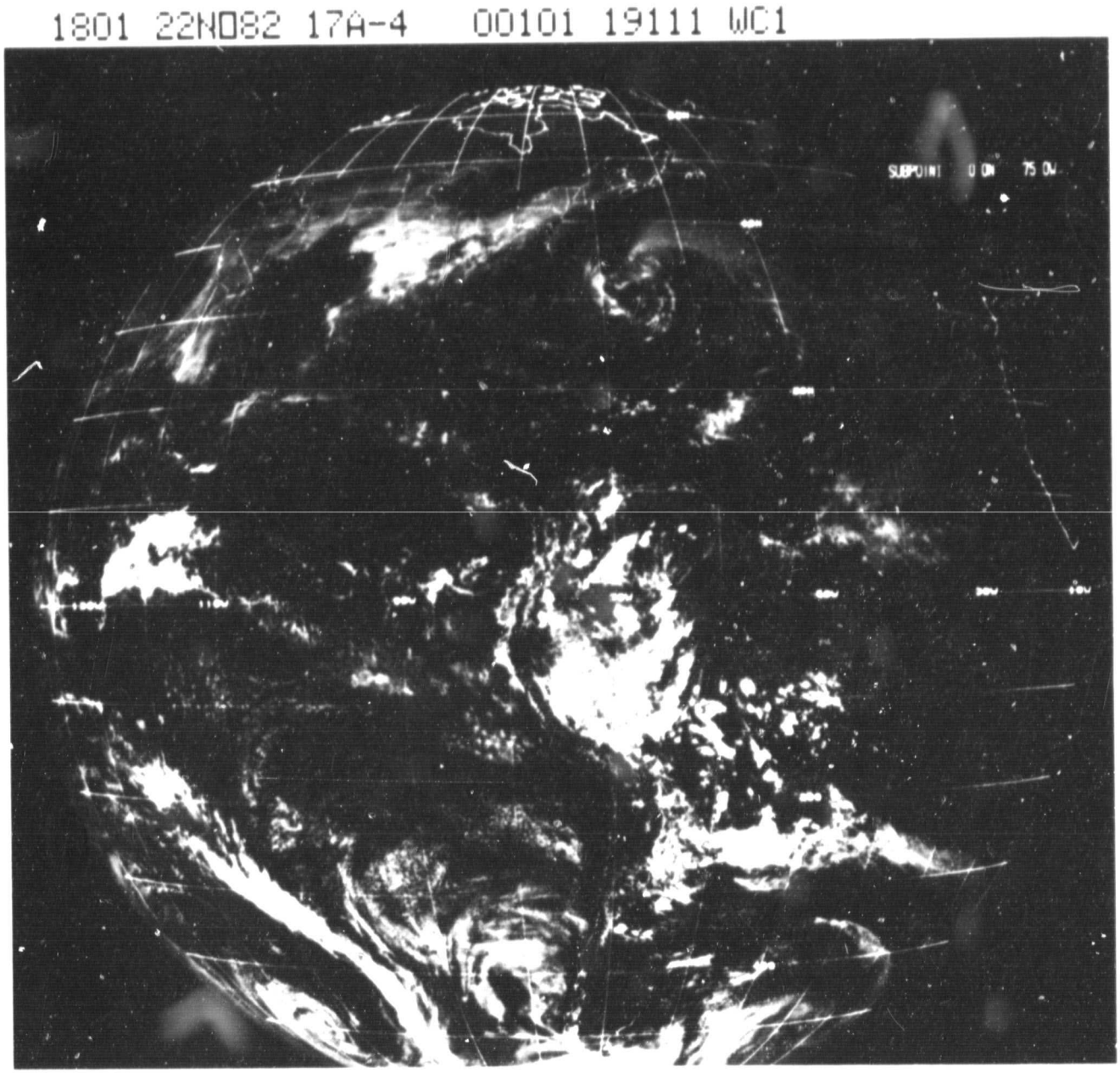

Figure 27. Raw visible GOES image for SPADS cases A and B

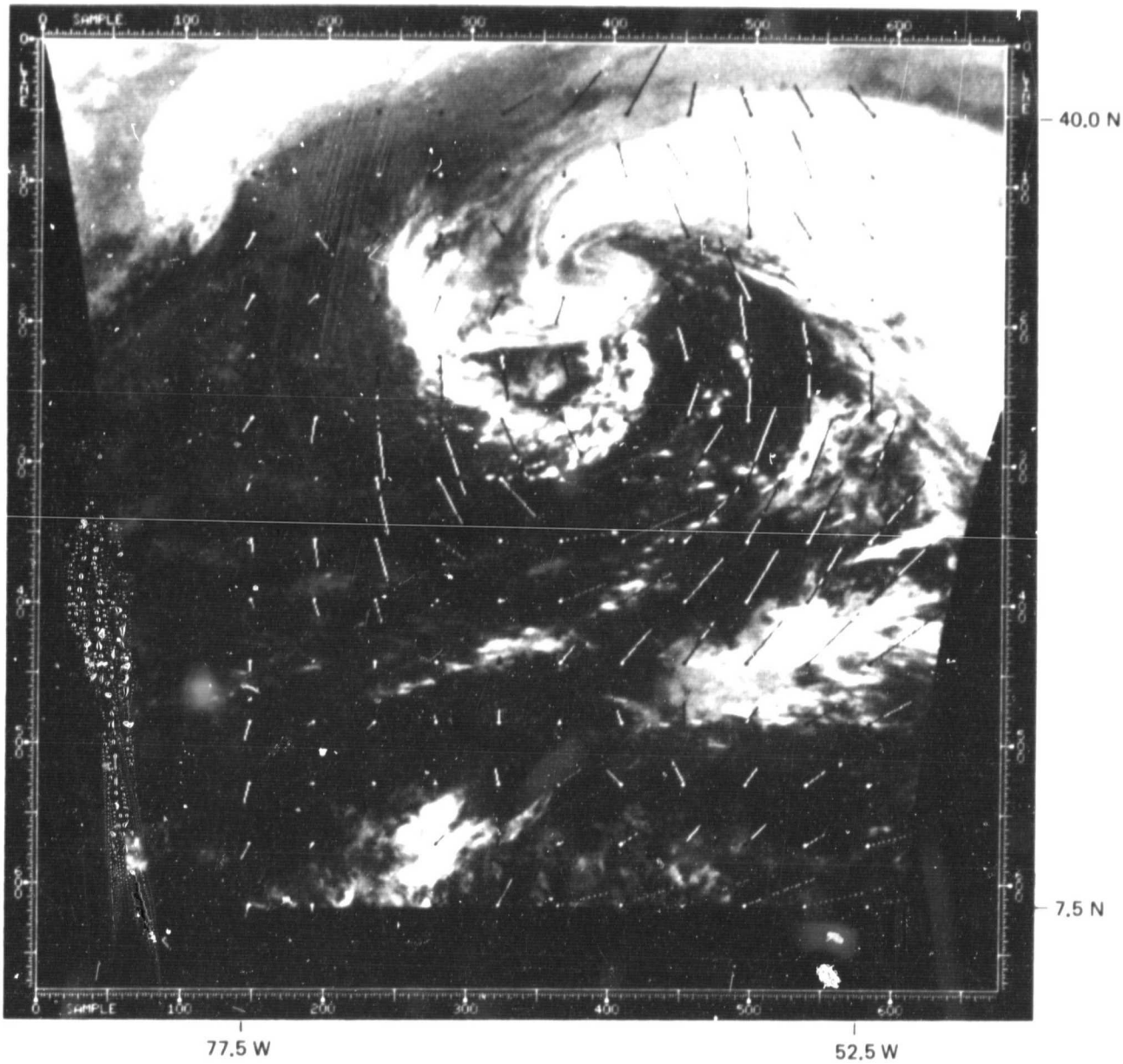

Figure 28. Veered SPADS winds for case A, Nov 22, 1982

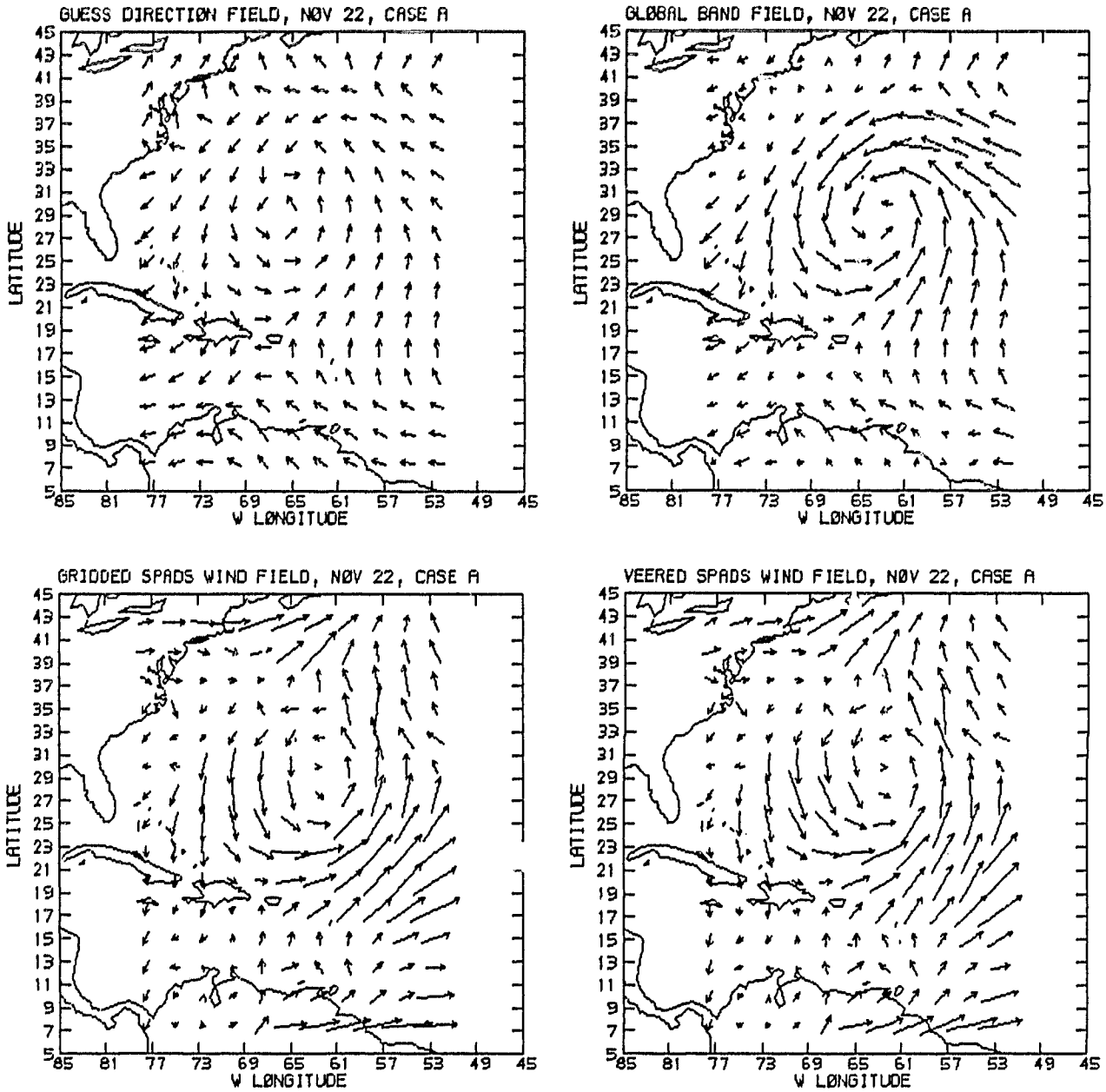

Figure 29. Wind vector plots for SPADS case A, Nov 22, 1982

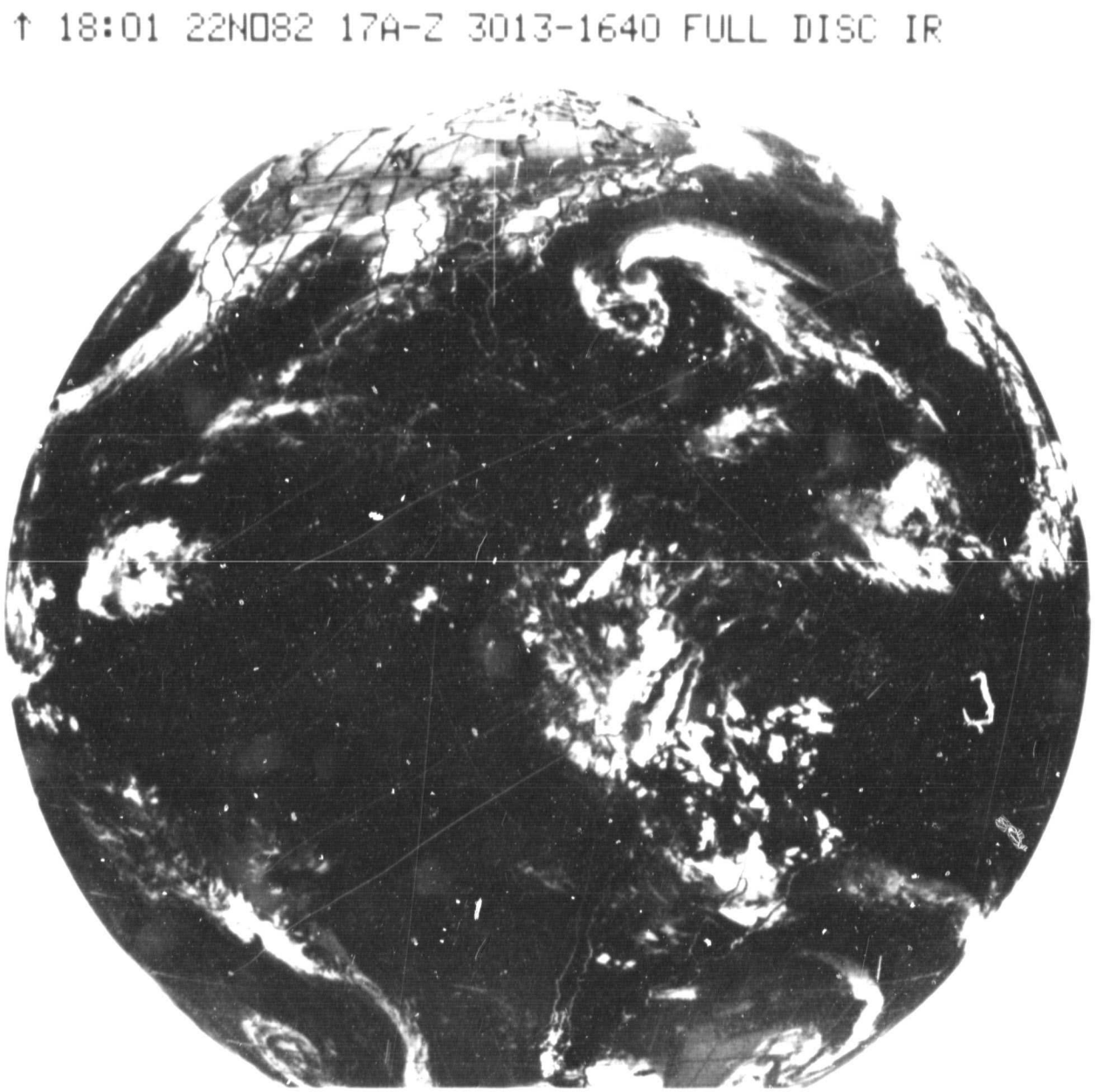

Figure 30. Raw IR GOES image for SPADS cases A and B

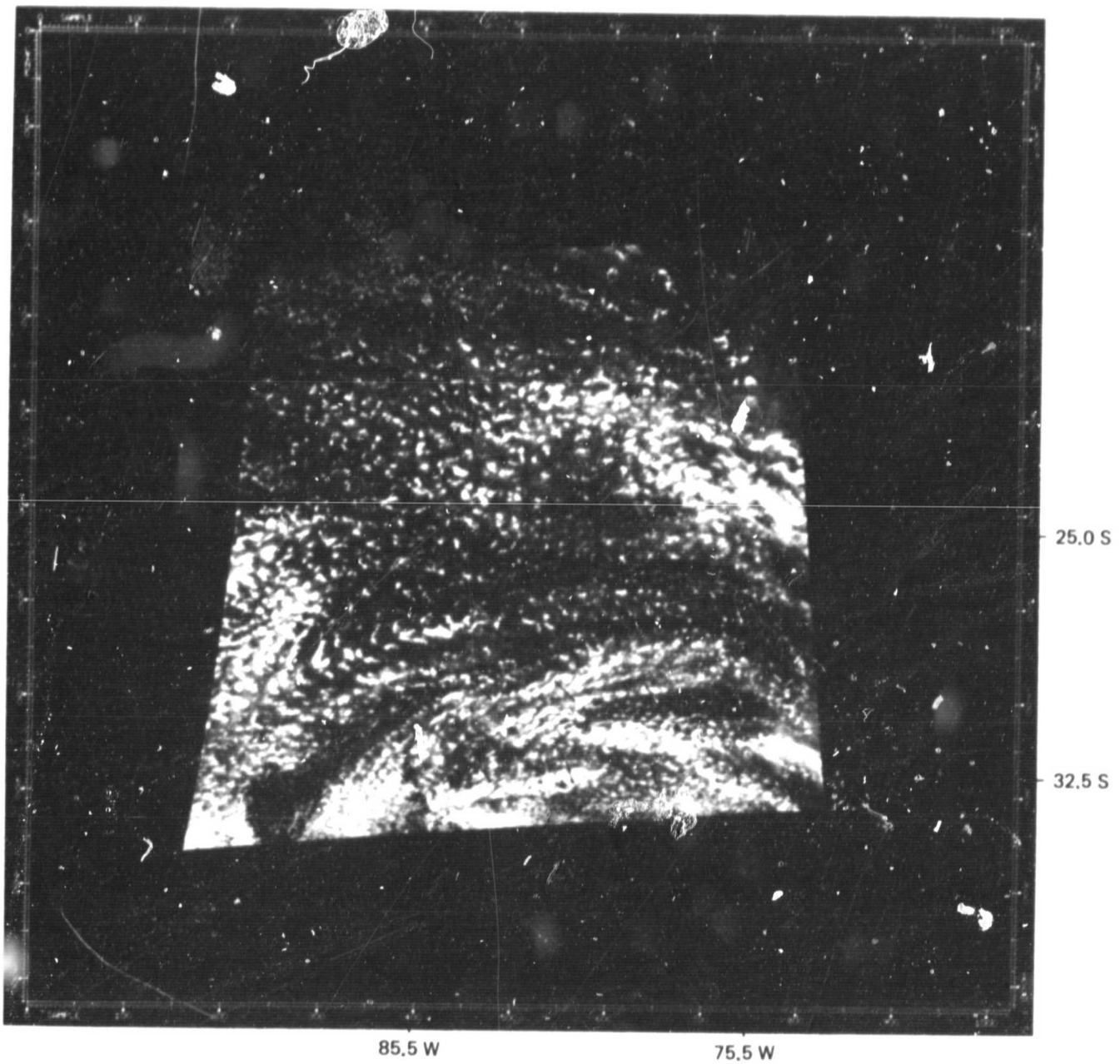

Figure 31. Veered SPADS winds for case B, Nov 22, 1982

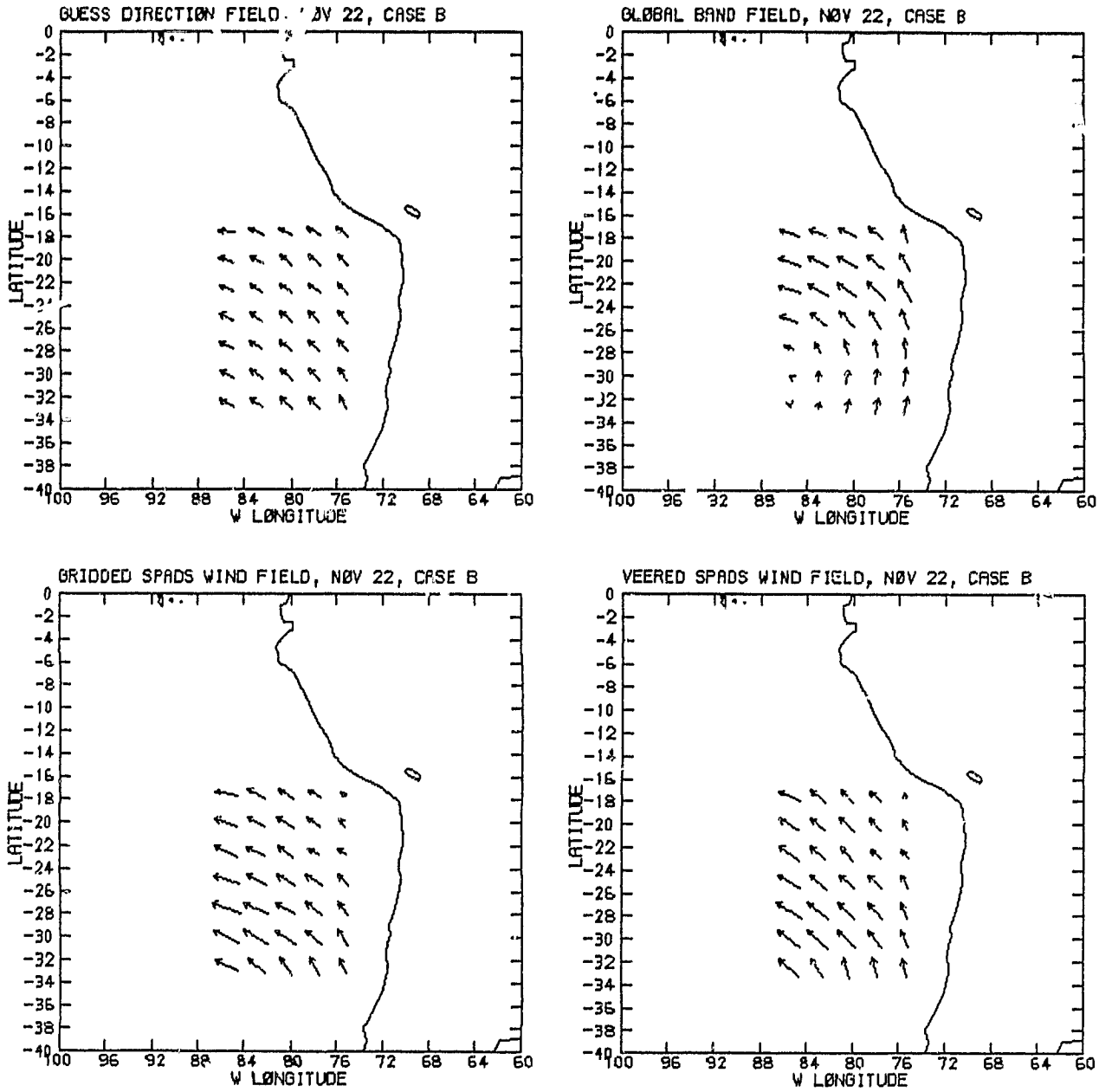

Figure 32. Wind vector plots for SPADS case B, Nov 22, 1982

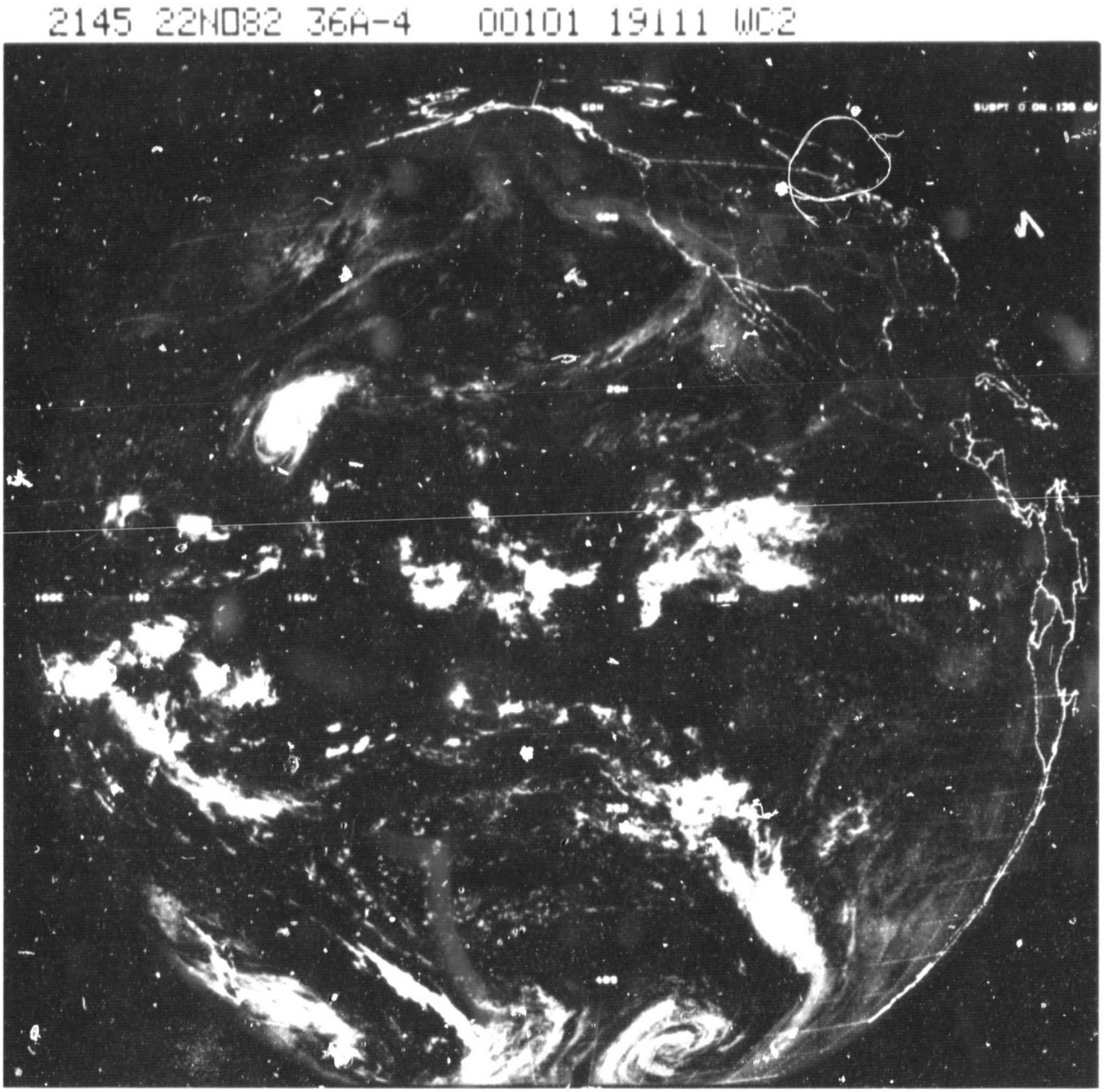

Figure 33. Raw visible GOES image for SPADS cases C and D

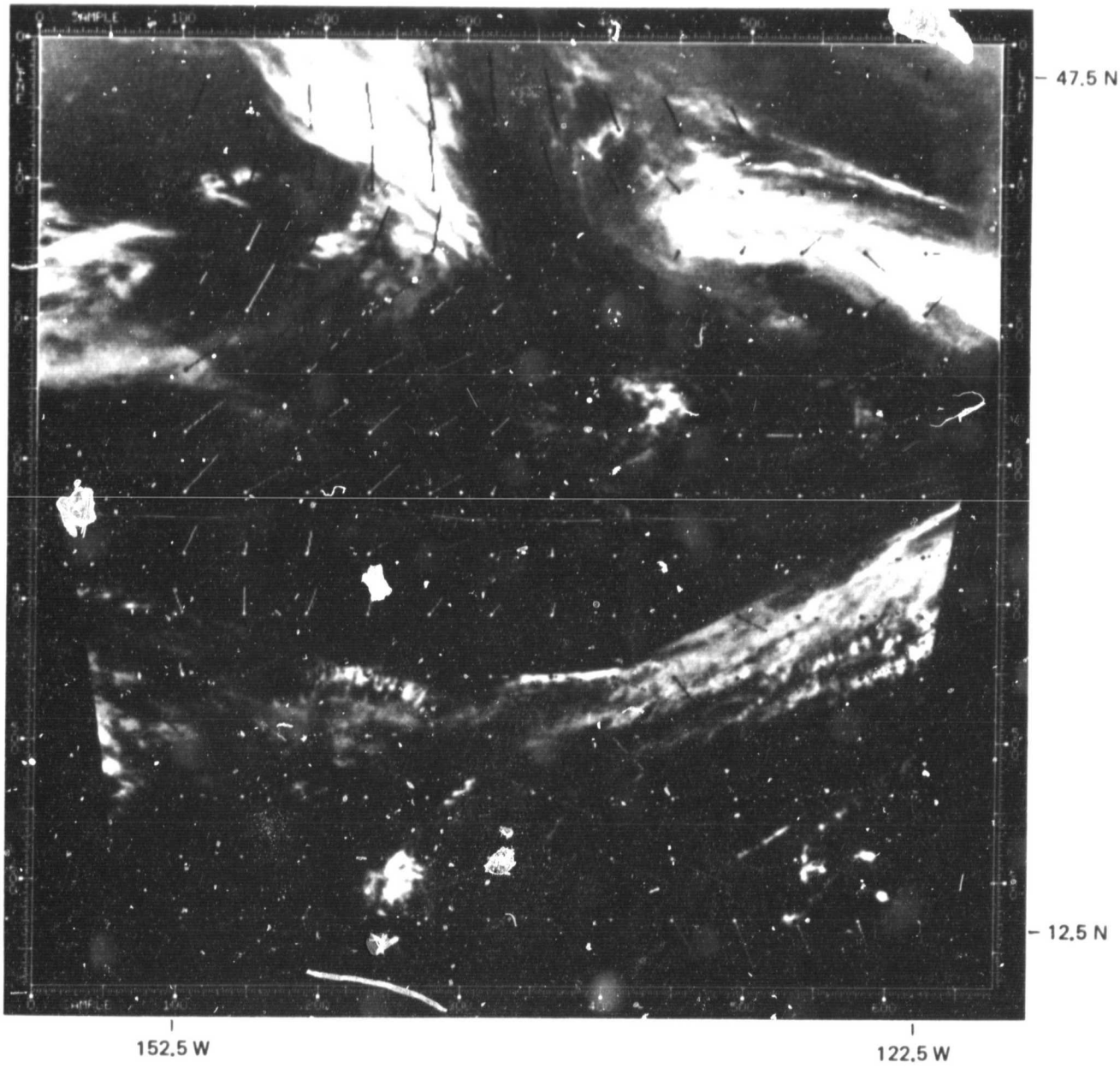

Figure 34. Veered SPADS winds for case C, Nov 22, 1982

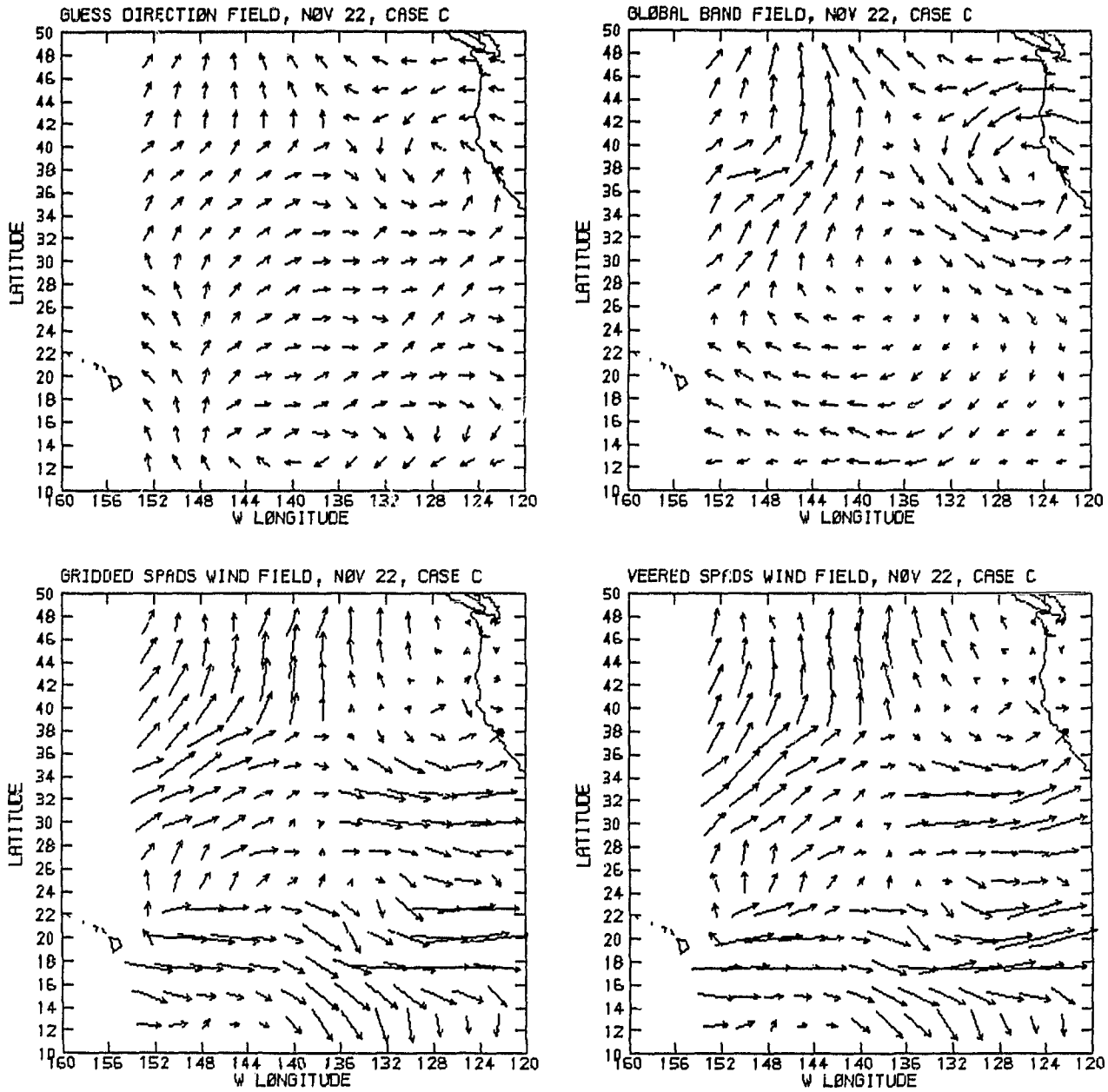

Figure 35. Wind vector plots for SPADS case C, Nov 22, 1982

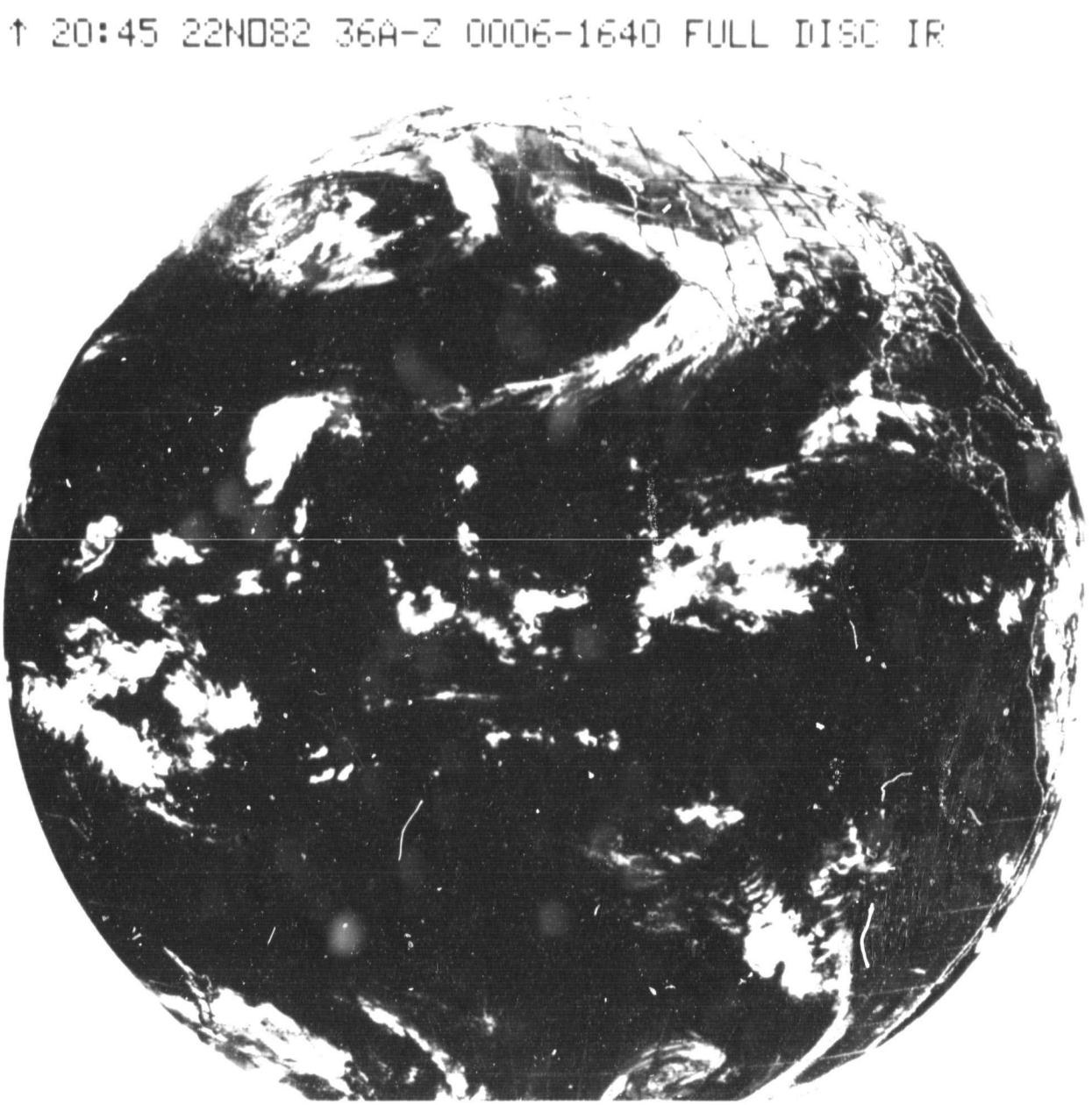

Figure 36. Raw IR GOES image for SPADS cases C and D

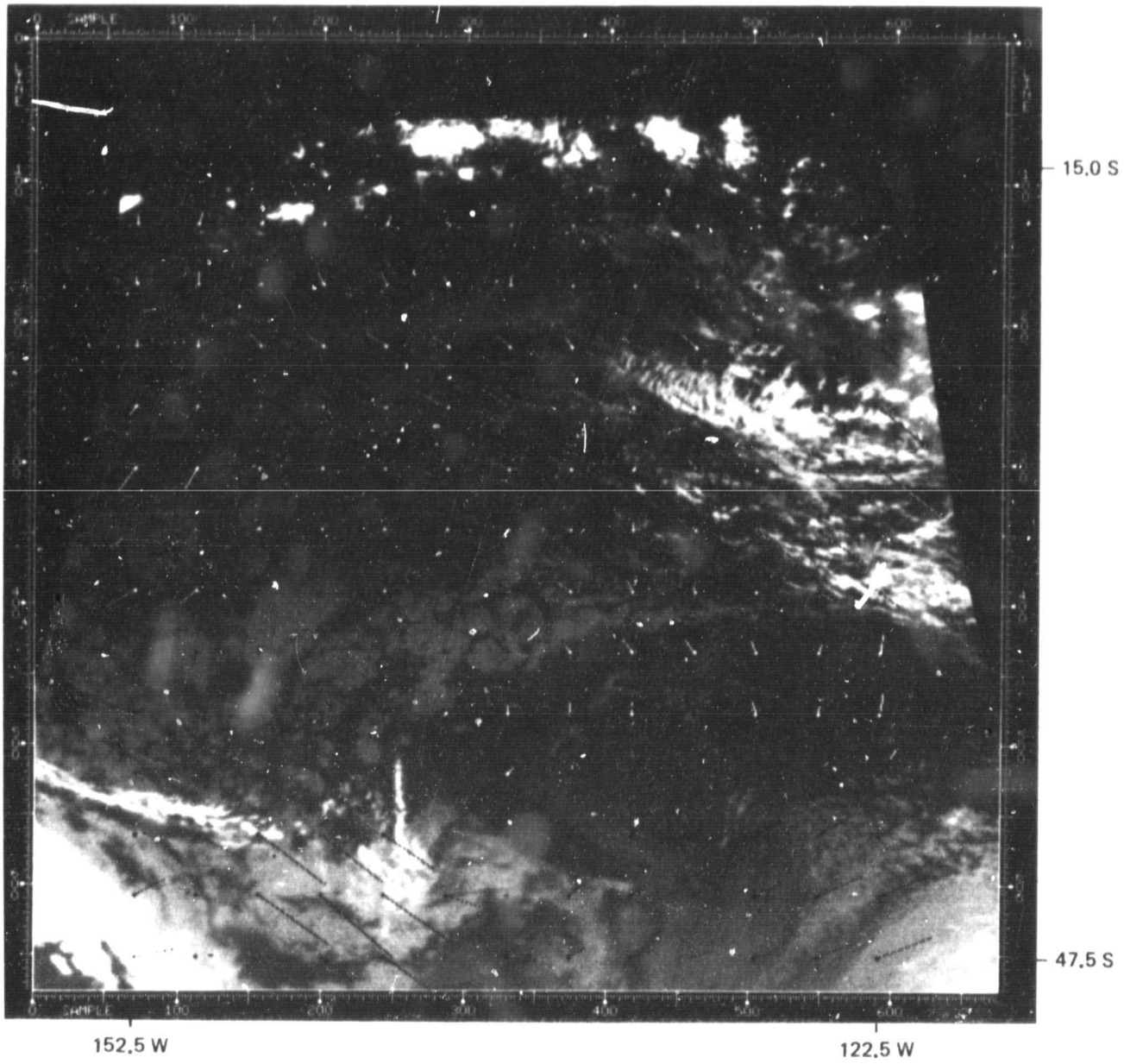

Figure 37. Veered SPADS winds for case D, Nov 22, 1982

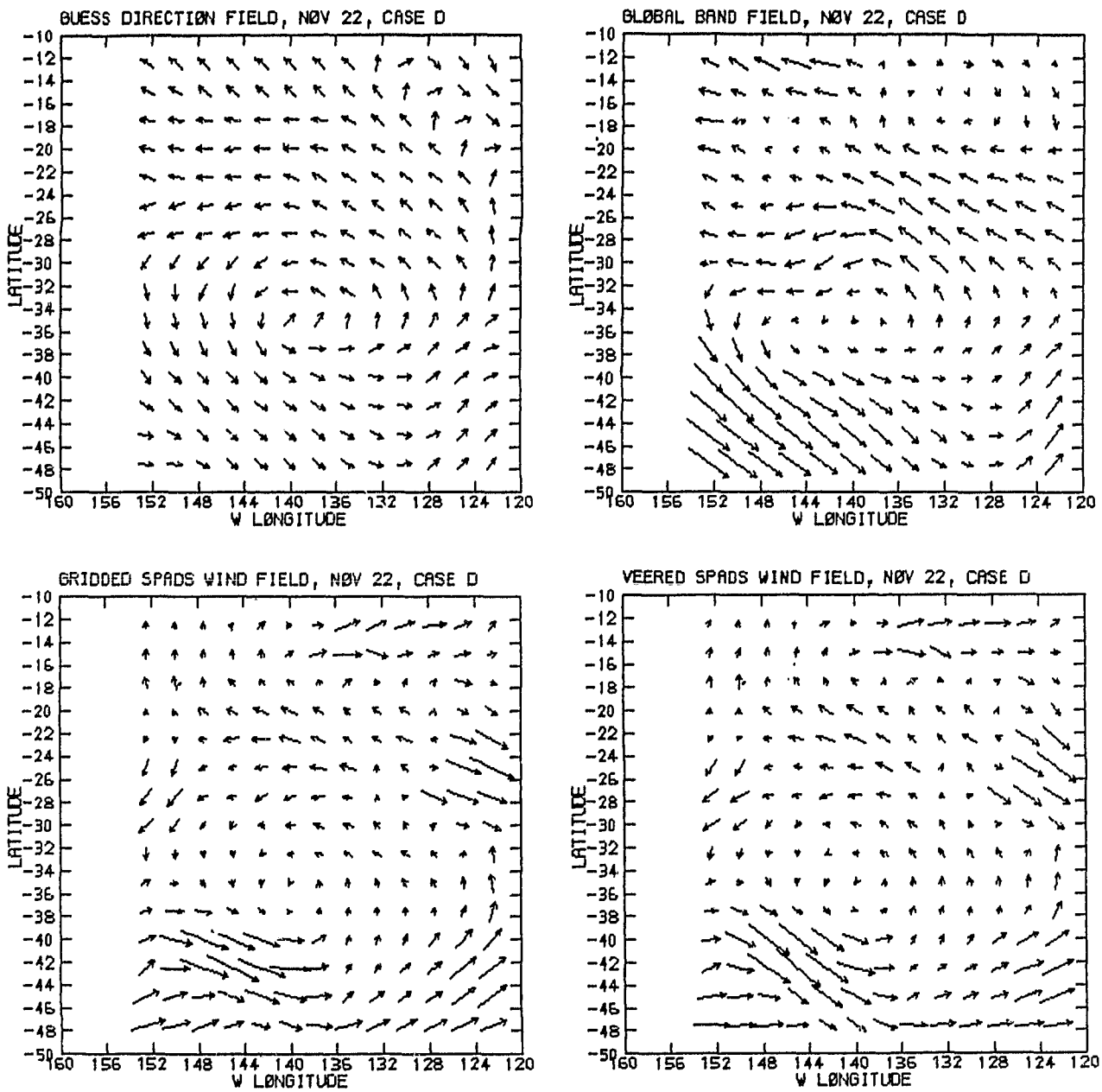

Figure 38. Wind vector plots for SPADS case D, Nov 22, 1982

SECTION 8

CONCLUSIONS

The cornerstone of this project is the wind veering algorithm, which permits extrapolation of the wind direction at the cloud level to the sea surface. This direction, when attached to the SSM/I speed, will provide the basis for the use of data from available satellite sensors in the FNOC operational weather models. A veering algorithm has been developed which is well suited to this project, relies only on available data, and accounts for the major physical phenomena involved. It represents what seems to be the optimal solution available with existing data.

The analysis of the disparate data types in this project requires their interpolation to a common geographical grid. The objective analysis method chosen functions well and is well suited to the task.

Originally, the constraints on the selection of test cases for this project were the concurrent availability of GOES VISSR imagery, NOAA/NESS cloud-tracked winds, global band fields, sea surface temperature, and Nimbus-7 SMMR surface wind speeds. Owing to the erratic availability of one or more of these products, the number of test cases became quite limited. At a fairly late stage, it became clear that one of the products, the Nimbus-7 SMMR wind speeds, would not be available at all for this project. With this constraint now removed, NEPRF provided four additional test cases utilizing the NEPRF SPADS cloud tracking system, making a total of nine test cases. Emphasis was now placed on studying the effects of the veering algorithm, with surface wind speeds to be attached to the veered wind directions at some later date.

To examine the effect of the veering on the cloud-tracked winds, a best-guess "surface truth" wind field was defined for each test case, based on the surface wind global band field, GOES visible and IR imagery, and meteorological intuition. The unveered and veered cloud wind fields were then subjectively compared to the guess field to determine whether the effect of the veering was beneficial, detrimental, or neutral. Vorticity and divergence fields reconstructed from the wind fields were also compared. The fact that the raw cloud wind fields were occasionally lacking data in important areas, or were tracking clouds at too high a level, had to be taken into consideration.

In general, for the limited number of test cases which we examined, the effect of the veering was beneficial, and in no case was highly detrimental. The cases spanned a variety of meteorological conditions including fronts, tropical and extratropical cyclones, anticyclones, trade winds, and the intertropical convergence zone. Normally, when new physical information is added to existing meteorological analysis, the impact is not overwhelmingly positive or negative. For the nine cases, the impact was judged to be positive for four, negative for two, and neutral for three. In terms of consistency, the impact is most positive in regions of extratropical cyclones and the ITCZ, and most negative around large anticyclones.

Generally, the veering correction for these cases was strongly dependent on latitude only, except in the vicinity of extratropical lows, where there were major perturbations and in which the highest positive impact was observed. Future research should be directed toward increasing the coefficient of the advection term in Equation (4), in order to determine if increasing the relative contribution of SST gradients has a beneficial effect on the results.

REFERENCES

Brown, R. A., 1982, private communication.

Brown, R. A. and Liu, W. T., 1982 "An Operational Large-Scale Marine Planetary Boundary Layer Model," Journal of Applied Meterology 21 (March), pp 261-269.

Cardone, V. J., 1969, "Specification of the Wind Distribution in the Marine Boundary Layer for Wave Forecasting," Report TR-69-1, Geophys. Sci. Lab. Available from NTIS AD#702-490. New York University, N.Y., N.Y.

Caton, F. G., Cuming, M. J. and Mendenhall, B. R., 1978, A Northern Hemisphere History of Marine Wind-Based Parameters, Meteorology International Incorporated, Monterey, Calif., MII Project M-231.

Chelton, D. B., 1982a, private communication.

Chelton, D. B., 1982b, "A Review of Techniques for Statistical Analysis of Long Time Series," unpublished manuscript.

Clarke, R. H. and Hess, G. D., 1975, "On the Relation Between Surface Wind and Pressure Gradient, Especially in Lower Latitudes," Boundary Layer Meteorology 9, pp 325-339.

Emmerson, S. R., 1979, "Intercomparison Between Objectively Analyzed Low Cloud-level Winds and Observed Surface Winds for the GATE Area," M. Sc. Thesis, U. Miami, Fla.

Endich, R. M. and Mancuso, R. L., 1968, "Objective Analysis of Environmental Conditions Associated with Severe Thunderstorms and Tornadoes," Monthly Weather Review 96 No. 6 pp 342-350.

Enfield, D. B., 1981, "Annual and Nonseasonal Variability of Monthly Low-Level Wind Fields Over the Southeastern Tropical Pacific," Monthly Weather Review 109, (October), pp. 2177-2190.

Gandin, L. S., 1965, Objective Analysis of Meteorological Fields, Israel Program for Scientific Translations, Jerusalem.

Gray, W. M., 1968, "Global View of the Origin of Tropical Disturbances and Storms," Monthly Weather Review 96, (October), pp 669-700.

Gray, W. M., 1972, A Diagnostic Study of the Planetary Boundary Layer Over the Oceans, Department of Atmospheric Science, Colorado State University, Atmospheric Science Paper No. 179.

Gray, W. M., 1982, private communication.

Halpern, D., 1979, "Surface Wind Measurements and Low-Level Cloud Motion Vectors Near the Intertropical Convergence Zone in the Central Pacific Ocean from November 1977 to March 1978," Monthly Weather Review 107, (November), pp 1525-1534.

Halpern, D., 1980, "Correlation Studies Between Low-Level Cloud Motion Vectors and Surface Wind Measurements Near 0°, 110°W, During the Global Weather Experiment," Proceedings of a Workshop on Applications of Existing Satellite Data to the Study of the Ocean Surface Energetics, C. Gauthier, ed., University of Wisconsin - Madison, pp 109-117.

Halpern, D. and Knox, R. A., 1982, "Coherence Between Low-Level Cloud Motion Vectors and Surface Wind Measurements Near 0° 152°W from April 1979 - February 1980," preprint.

Janota, P., 1971, "An Empirical Study of the Planetary Boundary Layer in the Vicinity of the Intertropical Convergence Zone," Ph.D. Thesis, MIT Dept. of Meteorology, Boston, Mass.

Krishnamurti, T. N. and Krishnamurti, R., 1978, "Surface Meteorology over the GATE A-Scale," Tech. Rpt. 78-6, Dept. Meteor. Oceanogr., Fla. State University, Tallahassee, Fla.

Liu, W. T., 1982, private communication.

Mahrt, L. J., 1972, "A Numerical Study of the Influence of Advective Accelerations in an Idealized, Low-Latitude, Planetary Boundary Layer," Journal of the Atmospheric Sciences 29, (November), pp 1477-1484.

Mendenhall, B. R., 1967, A Statistical Study of Frictional Wind Veering in the Planetary Boundary Layer, Department of Atmospheric Science, Colorado State University, Atmospheric Science Paper, No. 116.

Mendenhall, B. R., Holl, M. M. and Cuming, M. J., 1977 Development of a Marine History of Analyzed Sea-Level Pressure Fields and Diagnosed Wind Fields, Meteorology International Incorporated, Monterey, Calif., MII Project M-227.

Mendenhall, B. R., 1982, private communication.

Pazan, S., 1982, private communication.

Pihos, G. G., 1982, JPL IOM "Algorithms for Producing Gridded Seasat SASS, SMMR and VIRR Data Sets", Jet Propulsion Laboratory, Pasadena, Calif. (JPL internal document).

Robitaille, F. E. and Zipser, E. J., 1970, "Atmospheric Boundary Layer Circulations Equatorward of the Intertropical Convergence Zone," Preprints of Papers, Symp. on Tropical Meteorology, Amer. Meteor. Soc. CIV-1 to 6.

Sadler, J. C., 1982, private communication.

Sadler, J. C., 1984, private communication.

Sadler, J. C. and Kilonsky, B. J., 1981a, Trade Wind Monitoring Using Shuttle Experiment Observations, Department of Meteorology, University of Hawaii, UKHMET 81-01.

Sadler, J. C. and Kilonsky, B. J., 1981b, Meteorology During the Test Shuttle Experiment, Department of Meteorology, University of Hawaii, UHMET 81-05.

Schott, F. and Fernandez-Partagas, J., 1981, "The Onset of the Summer Monsoon During the FGGE 1979 Experiment off the East African Coast: A Comparison of Wind Data Collected by Different Means," Journal of Geophysical Research 86, (May), 4173-4180.

Willebrand, J., 1978, "Temporal and Spatial Scales of the Wind Field Over the North Pacific and North Atlantic," Journal of Physical Oceanography 8, pp 1080-1094.

Wylie, D. P., 1982, private communication.

Wylie, D. P. and Hinton, B. B., 1981, "The Feasibility of Estimating Large-Scale Surface Wind Fields for the Summer MONEX Using Cloud Motion and Ship Data," Boundary Layer Meteorology 21, pp 357-367.

Wylie, D. P. and Hinton, B. B., 1982a, "The Wind Stress Patterns Over the Indian Ocean During the Summer Monsoon of 1979," Journal of Physical Oceanography 12, p. 186.

Wylie, D. P. and Hinton, B. B., 1982b, "A Comparison of Cloud Motion and Ship Wind Observations Over the Indian Ocean for the Year of FGGE," Boundary Layer Meterology 23, pp. 197-208.